MODELING AND PERFORMANCE EVALUATION
OF AN ORGANIC RANKINE CYCLE (ORC)
WITH R245FA AS WORKING FLUID

A THESIS SUBMITTED TO
THE BOARD OF CAMPUS GRADUATE PROGRAMS OF
MIDDLE EAST TECHNICAL UNIVERSITY,
NORTHERN CYPRUS CAMPUS

BY

MUSBAUDEEN OLADIRAN BAMGBOPA

IN PARTIAL FULLFILLMENT OF THE REQUIREMENTS
FOR
THE DEGREE OF MASTER'S OF SCIENCE
IN
SUSTAINABLE ENVIRONMENT AND ENERGY SYSTEMS

MAY 2012

Approval of the thesis:

MODELING AND PERFORMANCE EVALUATION OF AN ORGANIC RANKINE CYCLE (ORC) WITH R245FA AS WORKING FLUID

submitted by **MUSBAUDEEN O. BAMGBOPA** in partial fulfilment of the requirements for degree of **Master's of Science in Sustainable Environment and Energy Systems (SEES) program, Middle East Technical University, Northern Cyprus Campus (METU-NCC)** by,

Prof. Dr. Erol Taymaz   _____
Chair of the **Board of Graduate Programs**

Asst. Prof. Dr. Ali Muhtaroğlu   _____
Program coordinator, **SEES program**

Asst. Prof. Dr. Eray Uzgören   _____
Supervisor, **Mechanical Engineering Dept.**

Examining Committee Members:

Prof. Dr. Rüknettin Oskay   _____
Mechanical Engineering Dept., METU

Asst. Prof. Dr. Eray Uzgören   _____
Mechanical Engineering Dept., METU-NCC

Asst. Prof. Dr. Ali Muhtaroğlu   _____
Electrical Engineering Dept., METU-NCC

Date: May 18th, 2012

I hereby declare that all information in this document has been obtained and presented in accordance with academic rules and ethical conduct. I also declare that, as required by these rules and conduct, I have fully cited and referenced all material and results that are not original to this work.

Name, Last name :

Signature　　　　　 :

ABSTRACT

This thesis presents numerical modelling and analysis of a solar Organic Rankine Cycle (ORC) for electricity generation. A regression based approach is used for the working fluid property calculations. Models of the unit's sub-components (pump, evaporator, expander and condenser) are also established. Steady and transient models are developed and analyzed because the unit is considered to work with stable (i.e. solar + boiler) or variable (i.e. solar only) heat input. The unit's heat exchangers (evaporator and condenser) have been identified as critical for the applicable method of analysis (steady or transient). The considered heat resource into the ORC is in the form of solar heated water, which varies between 80-95 ^{0}C at a range of mass flow rates between 2-12 kg/s. Simulation results of steady state operation using the developed model shows a maximum power output of around 40 kW. In the defined operation range; refrigerant mass flow rate, hot water mass flow rate and hot water temperature in the system are identified as critical parameters to optimize the power production and the cycle efficiency. The potential benefit of controlling these critical parameters is demonstrated for reliable ORC operation and optimum power production. It is also seen that simulation of the unit's *dynamics* using the transient model is imperative when variable heat input is involved, due to the fact that maximum energy recovery is the aim with any given level of heat input.

Keywords: Organic Rankine cycle, R245fa, transient modelling, phase change heat transfer

ÖZ

Bu tezin amacı, sayısal yöntem kullanarak Güneş enerjisi ile elektrik üretebilen Organik Rankin Çevrimi'nin (ORC) analizini yapmaktır. Bunun için; çevrim akışkanının regresyon temelli bir yaklaşım ile özelliklerinin hesaplanması ve sistemin alt bileşenlerinin (pompa, buharlaştırıcı, genleşletirici ve kondenser) ayrı ayrı modellenmesi öngörülmüştür. Isı girişinin kararlı (Güneş enerjisi kazan ile birlikte kullanıldığında) veya değişken (yalnız Güneş enerjisi) olması durumu göz önüne alınarak, sistemin kararlı ve zamana bağlı durumları için iki ayrı yöntem geliştirilmiş ve bu koşullara bağlı analizi yapılmıştır. Bu yöntemler (kararlı veya geçici), esas olarak ısı değiştiricilerin (buharlaştırıcı ve kondenser) temel alınması tespit edilmiştir. ORC'ye giren ısı kaynağı; kütle akış hızı 2-12 kg/s aralığında ve sıcaklığı 80-95 ^{o}C aralığında değişen Güneş enerjisi ile ısıtılmış su ile sağlandığı düşünülmüştür. Geliştirilen yöntemler kullanılarak yapılan hesaplamalar, seçilen koşulların kararlı durum için en fazla 40 kW'lık elektrik elde edilebileceğini göstermiştir. Sistemin geçici durumdan kararlı hale geçebilmesi için önemli olabilecek değişkenler; ORC'deki akışkan debisi, sıcak su döngüsünün debisi ve sıcak suyun buharlaştırıcıya giriş sıcaklığı alınmıştır. Bu önemli değişkenlerin kontrolü ile sistemin optimum ve kararlı güç üretimi sağlayabildiği gösterilmiştir. Ayrıca, değişken ısı girişi söz konusu olduğunda, benzetim yoluyla elde edilen sistem dinamikleri sayesinde en fazla güç kazanımının tespit edilmesi için geçici yöntem kullanılmasının şart olduğunu göstermektedir.

Anahtar Kelimeler: Organik Rankine çevrimi, R245fa, geçici ısı aktarımı yöntemleri, faz değişimli ısı aktarımı

DEDICATION

With praises to the 'great geometrician of the universe', I dedicate this work to my family and to everybody who has contributed towards my development so far.

ACKNOWLEDGEMENT

The author wishes to recognise the support of the thesis supervisor; Asst. Prof. Dr. Eray Uzgören for his technical support and assistance to steer the research to completion.

TABLE OF CONTENTS

LIST OF TABLES

LIST OF FIGURES

NOMENCLATURE

A:	area, (m^2)		**Greek symbols**	
C_p:	specific heat capacity, (J/kg. ^{0}C)	ρ:	density, (kg/m^3)	
d:	diameter, (m)	μ:	viscosity, (Pa.s)	
E:	energy, (J)	ε:	effectiveness	
g:	acceleration due to gravity, (m/s^2)	η:	efficiency	
h:	enthalpy, (kJ/kg)			
H:	heat transfer coefficient (W/m^2.K)			
k:	thermal conductivity, (W/m.K)		**Subscripts**	
$\dot{m}$:	mass flow rate, (kg/s)	b:	boiling	
NTU:	number of transfer units	c:	condensation	
P:	pressure, (Pa)	co:	condenser	
Pr:	Prandtl number	em:	electromechanical	
Re:	Reynold's number	ev:	evaporator	
q:	specific heat, (J/kg)	exp:	expander	
$\dot{Q}$:	heat rate, (W)	f:	fluid	
t:	time (sec)	l:	liquid	
T:	temperature, (^{0}C)	min/max:	minimum/maximum	
U:	overall heat transfer coefficient, (W/m^2.K)	pu:	pump	
$\dot{V}$:	volume flow rate, (m^3/s)	ref:	refrigerant	
w:	specific work/heat, (J/kg)	sat:	saturated	
$\dot{W}$:	work rate, (W)	v:	vapour	
x:	vapour quality	w:	water	

CHAPTER 1

1. INTRODUCTION

The dilemma of increasing energy demand with a decrease in reserves of widely used fossil fuels, the negative effects of traditional energy use on the climate demands exploring sustainable sources of energy. Over the years, petroleum (crude oil and natural gas) continued to be the world's most important primary energy source. It can be seen from recent available statistics [1] that in the United states, a major world energy consumer, crude oil accounts for about 37% of total energy consumption with a trend of 2.4% annual increase. Crude oil is followed by natural gas (25%) and coal (21%).

In recent years, more attention is devoted to alternative sources of energy; especially with the focus of geothermal, solar, and wind. Among these, solar energy is the one appealing to scientists for investigating the effective use of this free, inexhaustible, naturally occurring but intermittent energy. It can also be said that solar energy is the one with more predictable output in its wide range of applications. Solar energy technologies appear in many applications including "solar for agriculture"; in poultry brooding and food drying [2]. Solar-lighting systems involve active and passive interior lighting provided by sunlight through optical devices [3]. Solar photovoltaic systems use photovoltaic cells are used for distributed electricity generation [4], and "solar-thermal systems

Solar-thermal systems are classified as the systems which directly utilize the thermal energy from solar radiation. Common applications include solar heating and cooling using solar heaters and sorption systems for space conditioning [5], solar desalination where solar energy is the heat input to the cycle that drives desalination pumps [6], and solar-thermal electricity [7].

The idea behind solar thermal electricity generation usually involves using solar energy to supply some or all of the thermal energy required to drive thermal power systems, mostly steam power engines (Rankine cycles). Central receiver systems and heliostats are capable of providing temperatures high enough to operate Rankine cycles. However, some of them are not fully commercialized options, and there is a claim that these high temperature Rankine cycles are not economic in small scale applications [8]. The purpose of the present

study is to investigate the applicability of the Organic Rankine Cycle (ORC) for small-scale power generation utilizing low-grade heat sources from solar radiation.

1.1. Organic Rankine Cycles

The Rankine cycle itself is named after one of the founding contributors to the science of thermodynamics; William John Macquorn Rankine (1820 - 1872), a Scottish engineer and physicist who is also credited for the 'Rankine' temperature scale. In an effort to experiment with different working fluids, Frank Ofeldt in 1883 developed a steam power engine that worked with naphtha (a distillation product from petroleum). The technology of ORC was later to be utilized in the 20th century [9]. It can be said that the birth of the ORC was as a result of the desire to use different working fluids which are more volatile than water. ORCs have recently become a very attractive option to harness electricity from low-grade heat sources especially after the development of suitable working fluids to replace water in traditional Rankine cycles [10]. Energy conversion from low temperature heat sources becomes possible through the use of these organic fluids, which are usually in the form of chloro-fluoro-carbons (CFC), hydro-chloro-fluoro-carbons (HCFC) and hydro-fluoro-carbons (HFC) [8].

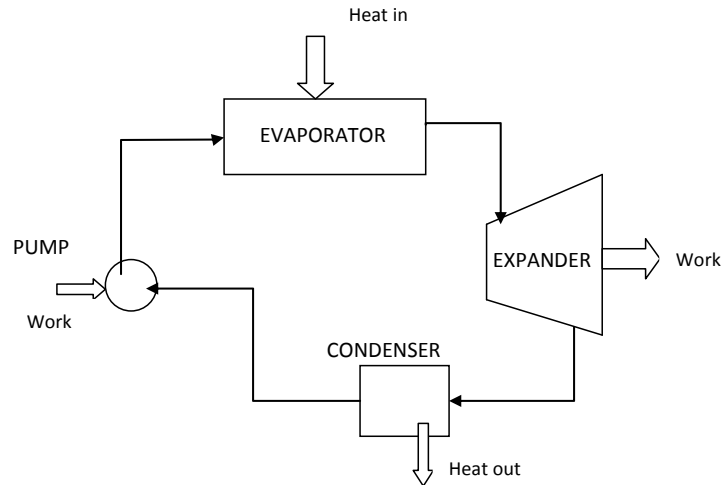Figure 1: Representation of a Rankine cycle.

Recent commercial ORCs are becoming smaller (on power output) as compared to conventional Rankine cycles (RCs) [11] to make them suitable for a wide range of applications. Depicting similarity to a conventional Rankine cycle, a schematic representation of a typical ORC is shown in Figure 1. In a typical Rankine cycle, liquid refrigerant is pumped

2

from low pressure to a higher one before entering the evaporator where it gets hotter until reaches a vapour state. The vapour refrigerant is then expanded to the lower pressure by the expander to produce useful work. The refrigerant leaving the expander is then cooled at the same low pressure side of the cycle to complete the cycle. Replacing the boiler with an evaporator and turbine with an expander, ORCs are well suited for power generation using low temperature heat sources as compared to RCs but with lesser efficiencies (8-12% for the small scale systems) [12].

The low-grade heat input can be supplied through solar energy, biomass, geothermal, heat from internal combustion engines or waste heat from other industrial processes. This makes ORCs widely suitable in many heat recovery and CHP (combined heat and power) systems. The present study considers ORC application for a solar-thermal power production.

1.2. ORC Research

Since recent research has demonstrated ORCs are good candidates for power production (energy recovery) from low temperature heat sources (compared to water in the same operation temperature range) [13], various researchers have investigated the use of ORCs in several applications as discussed in a *state of the art* review of ORCs by Tchanche et al. [14]. Tchanche et al. in [15] also reviewed working fluids that have been considered for use in ORCs as they are the main distinguishing factor between ORCs and RCs. In the review in [14], it is seen that a larger literature base exists for ORC application in desalination compared to electricity generation.

One major challenge in analyzing/modelling solar ORC systems (especially for electricity generation) is the variability of the available heat input due to intermittency of solar energy. In dealing with this challenge, considering a supplementary boiler (auxiliary heat input) in the analysis would help ensure stable input conditions as assumed in the studies of Delgado-Torres & García-Rodríguez [16] and Roy et al. [17]. Such studies which assume steady heat input help present an overview of the ORC unit's performance as a function of identified critical parameters in the operating temperature range. However, in systems where this assumption does not apply, analyses have to be made based on transient models and state equations. This is the case for ORCs utilized in energy recovery from internal combustion (IC) engines and solar ORCs without supplementary boiler. Hence, the goal is usually to investigate the possible control strategies of critical parameters such as evaporating temperature, mass flow rates, etc. for optimum cycle performance as seen in Quoilin et. al. [18].

Therefore, modelling and performance analysis of an ORC unit, which operates solely on solar heat input or both solar and supplementary boiler heat input, should harmonize both methods of analysis (steady or transient) as the present study intends.

1.3. Objective of the Thesis

It is common knowledge amongst renewable energy professionals, as also stressed in [8], that solar thermal power cycles are not as competitive economically when compared to conventional thermal power plants if environmental externalities, which are challenging to quantify are not considered. This is the drive behind further investigation of the operation and optimization of these systems, including ORCs.

Present study draws inspiration from an ORC unit installed at the solar-thermal field of Middle East Technical University, Northern Cyprus Campus (METU NCC), designed and manufactured by ELECTRATHERM®. ELECTRATHERM's ORC is widely used with geothermal, biomass and industrial waste heat sources while its use with solar-thermal energy is limited to the case in Hawaii at 100 kWe [19]. The fundamental challenge (time-dependent behaviour of heat source) is not usually encountered in other common applications of ORC (with geothermal, biomass and industrial waste heat sources) as in solar.

The objective is to develop an ORC model and further investigate the ORC's performance with steady and variable low-grade heat source. The unique contribution of this work is the research on evaluation of ORC units (specifically in solar-thermal application) through modelling and identification of performance optimization potentials based on these models, as the particular installation which inspired this work is first of its kind in the location.

The thesis is organized in five chapters including the introduction Chapter which defines the problem and lays out the motivation for the present study. The second chapter presents the detailed model of the working fluid (R245fa) with the ORC application in focus. This is presented after briefly discussing refrigerants used in ORCs; the essential component differentiating ORCs and RCs. Third chapter presents the developed numerical model for the ORC as a synthesis of separately discussed sub-models for each main component of the system. Fourth chapter presents investigative studies performed at the system level. Finally, the last chapter presents conclusions from this thesis research, recommendations and a scope of further research related to this work.

CHAPTER 2

2. WORKING FLUID MODEL

Among the refrigerants commonly utilized in ORCs (i.e. chloro-fluoro-carbons (CFC), hydro-chloro-fluoro-carbons (HCFC) and hydro-fluoro-carbons (HFC)), CFCs have later been discovered to be environmentally unfriendly [20] and steps have been taken to discontinue their use or modify their composition. Environmental considerations include global warming potential (GWP), ozone layer depletion potential (ODP), toxicity, flammability etc. Wang et al. [21] highlights general properties of some of these fluids with no ODP as presented in Table 1 along with their GWP.

Table 1: Characteristics of certain working fluids as discussed in [12].

Refrigerant	Molar mass (g/mol)	Critical Temp. (^{0}C)	Critical Pressure (MPa)	GWP (100 years)
R134a	102.03	101.1	4.06	1300
R245fa	134.05	154.1	3.64	950
Ammonia	17.03	132.3	11.34	<1
Pentane	72.15	196.6	3.37	20

Considering their GWPs, fluids similar to R245fa have started to replace the earlier ones in many relevant industrial applications. The ORC system being investigated in this study also considers R245fa, which has the chemical nomenclature; HFC 1,1,1,3,3 pentafluoropropane according to the National Institute of Science and technology (NIST) [22].

In order to be able to investigate an Organic Rankine Cycle (ORC), the state properties of the working fluid, which is R245fa, are required to be evaluated around the saturated liquid-vapour region. The thermo physical and transport properties of R245fa as published by the manufacturer of the organic fluid are utilized for non-linear regression for subcooled liquid, saturated liquid-vapour mixture and superheated vapour regions (Figure 2). The nature of the correlations for each of these regions come from the ASHRAE research project 1256-RP [23], which provides the thermo-physical and transport properties of R245fa through direct measurement and analysis of experimental data. After extracting the correlation coefficients through a regression analysis, a MATLAB library is formed to detect the region given the

input parameters and use the region specific regression coefficients to evaluate a property at a particular state. Input parameters can be any two of the following thermo-physical properties: density, temperature, pressure, specific enthalpy, and specific entropy.
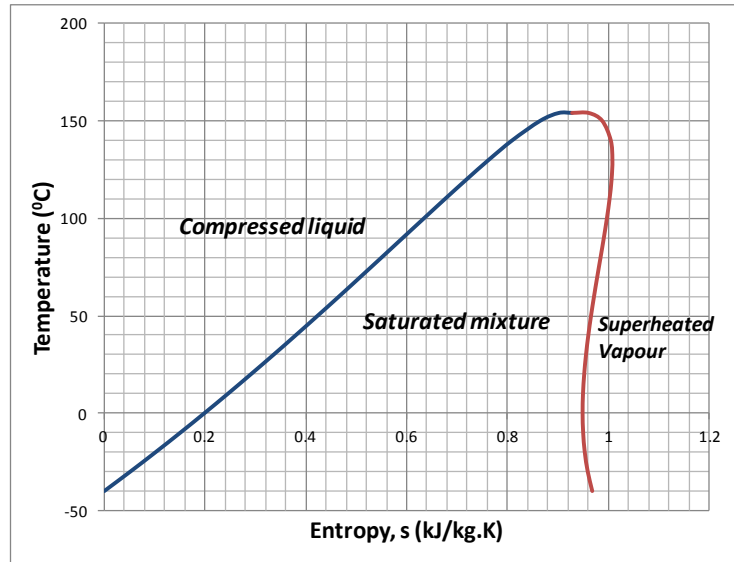
Figure 2: T-s diagram of R245fa.

Subsequent sections of this chapter will describe the models to evaluate the properties of (i) saturated mixture, (ii) compressed liquid, (iii) superheated vapour.

2.1. Saturated Properties

Saturation properties, i.e. density, specific enthalpy, specific entropy, are a function of either temperature or pressure. The saturation liquid and vapour curve for each of these properties can be obtained using piecewise regression method as a function of saturation temperature.

A sample property (for sat. liquid or sat. vapour) can be computed using Equation (1):

$$y = a_0 T^0 + a_1 T^1 + a_2 T^2 + \cdots + a_N T^N \tag{1}$$

where y represents the thermo-physical property, and a_0 to a_N are the regressed constants.

The first three terms are sufficient to mimic the data at the desired accuracy level. The non-linear regression is carried out by minimizing the mean of the square error (MSE) from each

Table 2: Regression coefficients for saturated properties of R245fa (10 ^{0}C - 40 ^{0}C).

Property		For 10^{0}C < T <= 40^{0}C			MSE	R^2
		a$_0$	a$_1$	a$_2$		
P$_{sat}$	(kPa)	7.95E- 2	1.61 E + 0	5.95 E + 1	2.10 E - 1	0.9999
$\rho_{sat,l}$	(kg/m^3)	-4.89E- 3	-2.46 E + 0	1.40 E + 3	8.12 E - 2	0.9999
$\rho_{sat,v}$	(kg/m^3)	4.61E- 3	7.42 E - 2	3.78 E + 0	1.78 E - 3	0.9999
h$_{sat,l}$	(kJ/kg)	1.09E- 3	1.29 E + 0	5.03 E + 1	9.01 E - 6	1.0000
h$_{sat,v}$	(kJ/kg)	-1.50E- 4	7.59 E - 1	2.55 E + 2	1.51 E - 5	1.0000
s$_{sat,l}$	(kJ/kg^{0}C)	-4.80E- 5	1.07 E - 2	8.13 E - 3	1.17 E - 4	0.9999
s$_{sat,v}$	(kJ/kg^{0}C)	-2.40E- 7	3.83 E - 4	9.45 E - 1	1.97 E - 7	0.9808
C$_{p,l}$	(kJ/kg^{0}C)	6.24E- 6	1.90 E - 3	1.29 E + 0	3.27 E - 7	0.9996
C$_{p,v}$	(kJ/kg^{0}C)	8.54E- 6	2.66 E - 3	8.36 E - 1	1.07 E - 7	0.9999
$\mu_{sat,l}$	(μPa.s)	3.99E- 2	-7.24 E + 0	5.62 E + 2	2.28 E - 1	0.9999
$\mu_{sat,v}$	(μPa.s)	1.49E- 5	3.26 E - 2	9.43 E + 0	1.24 E - 6	1.0000
k$_{sat,l}$	(W/m.K)	-1.40E- 7	-3.00 E - 4	9.76 E - 2	2.73 E - 9	0.9998
k$_{sat,v}$	(W/m.K)	-3.10E-6	2.79 E - 4	9.06 E - 3	2.15 E - 7	0.7759
$^*\sigma_{sat,l}$	(N/m)	-1.00E-5	3.08 E - 4	1.31 E - 2	1.28 E - 7	0.8391

Table 3: Regression coefficients for saturated properties of R245fa (40 ^{0}C - 94 ^{0}C).

Property		For 40^{0}C < T < 94^{0}C			MSE	R^2
		a$_0$	a$_1$	a$_2$		
P$_{sat}$	(kPa)	1.56 E -1	-5.41 E +0	2.23 E +2	5.23 E +0	0.9999
$\rho_{sat,l}$	(kg/m^3)	-9.76 E -3	-2.00 E +0	1.39 E +3	8.34 E -2	1.0000
$\rho_{sat,v}$	(kg/m^3)	9.70 E -3	-4.30 E -1	1.62 E +1	4.97 E -2	0.9998
h$_{sat,l}$	(kJ/kg)	1.64 E -3	1.23 E +0	5.15 E +1	5.15 E -4	1.0000
h$_{sat,v}$	(kJ/kg)	-9.90 E -4	8.41 E -1	2.53 E +2	1.15 E -3	1.0000
s$_{sat,l}$	(kJ/kg^{0}C)	-4.80 E -5	1.07 E -2	8.13 E -3	1.17 E -4	0.9750
s$_{sat,v}$	(kJ/kg^{0}C)	-2.30 E -5	3.77 E -3	8.34 E -1	3.25 E -5	0.6956
C$_{p,l}$	(kJ/kg^{0}C)	1.90 E -5	1.12 E -3	1.29 E +0	1.06 E -5	0.9967
C$_{p,v}$	(kJ/kg^{0}C)	9.40 E -6	3.19 E -3	8.09 E -1	3.01 E -5	0.9947
$\mu_{sat,l}$	(μPa.s)	1.68 E -2	-5.17 E +0	5.15 E +2	1.65 E -1	0.9999
$\mu_{sat,v}$	(μPa.s)	1.39 E -4	2.15 E -2	9.67 E +0	6.49 E -5	0.9998
k$_{sat,l}$	(W/m.K)	-2.20 E -5	2.69 E -3	8.28 E -5	2.73 E -5	-
k$_{sat,v}$	(W/m.K)	-2.40 E -6	4.35 E -4	1.22 E -5	4.66 E -7	0.8205
$^*\sigma_l$	(N/m)	-5.10 E -7	-9.50 E -5	1.76 E -2	4.82 E -7	-

* Liquid surface tension (σ_l) values were obtained from [22]

of the data set used for the regression and its corresponding actual value can be defined as in Equation (2).

$$MSE = \frac{\sum_i^N e_i^2}{N}, \quad \text{where } e_i = y_i - y_o \tag{2}$$

The number of data points, N have been set to at least 15 considering all properties were defined in three temperature ranges; $10\,^\circ\text{C} < T < 40\,^\circ\text{C}$, $40\,^\circ\text{C} < T < 94\,^\circ\text{C}$ and $94\,^\circ\text{C} < T < 130\,^\circ\text{C}$. These temperature ranges are known to be in the range of operation of the ORC, for higher temperatures up to the critical point, similar piecewise approach would be required for better definition of the whole *T-s* dome.

The accuracy of any correlation such as the developed ones can be checked by the square of correlation coefficient, calculated using Equation (3).

$$R^2 \cong 1 - \frac{MSE}{\text{var}(y_o)} \tag{3}$$

A perfect fit would produce a correlation coefficient of unity and worst fit would produce a correlation coefficient of zero [24]. Table 2 and Table 3 show the regressed constants for each of the given thermodynamic properties the MSE and correlation coefficient for two selected temperature ranges respectively.

Table 4 can help in comparison as it shows the results obtained for three different temperature values with their corresponding actual values.

2.2. Sub-cooled Liquid Properties

Following incompressible substance model, the specific internal energy and specific volume in the sub-cooled liquid state are approximated to the saturated properties at the same temperature [25].

$$u(T,P) \cong u_f(T), \quad v(T,P) \cong v_f(T) \tag{4}$$

For enthalpy, Equation (4) and the definition of the enthalpy can be utilized together.

$$h(T,P) \cong u_f(T) + v_f(T)(P - P_{sat}(T)) \tag{5}$$

Table 4: Errors in R245fa property calculations.

Property		T= 17^{0}C			T= 40^{0}C			T= 78^{0}C		
		Actual	Obtained	% error	Actual	Obtained	% error	Actual	Obtained	% error
P_{sat}	(kPa)	110.00	109.90	0.09	252.00	251.22	0.31	750.00	752.76	0.37
$\rho_{sat,l}$	(kg/m^3)	1360	1360.16	0.01	1297.00	1297.09	0.01	1177.00	1177.02	0.00
$\rho_{sat,v}$	(kg/m^3)	6.40	6.37	0.47	14.08	14.13	0.36	41.39	41.65	0.63
$h_{sat,l}$	(kJ/kg)	72.5	72.50	0.00	103.52	103.52	0.00	157.80	157.83	0.02
$h_{sat,v}$	(kJ/kg)	268.00	268.00	0.00	285.26	285.26	0.00	312.71	312.70	0.00
$s_{sat,l}$	(kJ/kg^{0}C)	0.2775	0.2773	0.07	0.3800	0.3796	0.11	0.5423	0.5503	1.48
$s_{sat,v}$	(kJ/kg^{0}C)	0.9513	0.9513	0.00	0.9604	0.9598	0.06	0.9835	0.9882	0.48
$C_{p,l}$	(kJ/kg^{0}C)	1.3222	1.3218	0.03	1.3732	1.3735	0.02	1.4912	1.494	0.19
$C_{p,v}$	(kJ/kg^{0}C)	0.8840	0.8837	0.03	0.9557	0.9560	0.03	1.1112	1.1148	0.32
$\mu_{sat,l}$	(μPa.s)	449.73	450.20	0.10	336.50	335.97	0.16	215.05	214.60	0.21
$\mu_{sat,v}$	(μPa.s)	9.99	9.99	0.00	10.76	10.76	0.00	12.18	12.19	0.08
$k_{sat,l}$	(W/m.K)	0.0925	0.0925	0.00	0.0854	0.0854	0.00	0.0740	0.0763	3.11
$k_{sat,v}$	(W/m.K)	0.0133	0.0129	3.01	0.0151	0.0153	1.32	0.0187	0.0193	3.21
$\sigma_{sat,l}$	(N/m)	0.0160	0.0154	3.75	0.0121	0.0130	7.14	0.0074	0.0071	4.05

Considering the ORC model, sub-cooled liquid state is expected to appear at the evaporator inlet. At this state, only specific enthalpy and pressure (marked as 2' in Figure 3) are known. The temperature at this state can be solved using Equation (5). As the specific enthalpy, specific internal energy and specific volume are evaluated using Equation (1), Equation (5) becomes a quadratic equation. Once the root for the temperature is found, other properties can be obtained by evaluating the saturated liquid properties at this temperature.
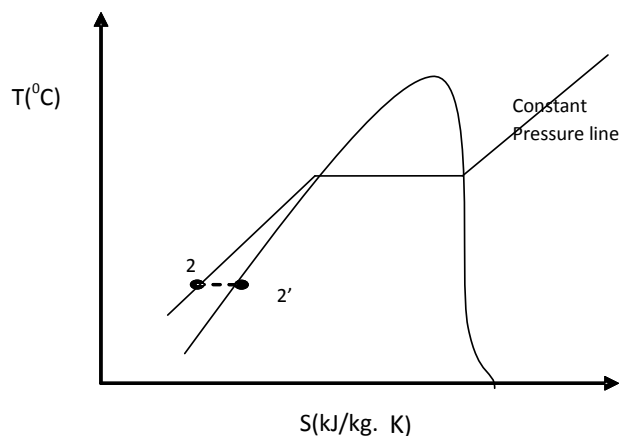

Figure 3: Obtaining sub-cooled liquid properties.

2.3. Superheated Properties

The properties at superheated region could not be approximated as those of the sub cooled region and cannot be solely defined in terms of temperature, this is because of their strong dependence on both temperature and pressure. Two methods have been considered to model enthalpy and entropy calculations for states in this region (there are other methods – i.e. Helmholtz equation [26]).

2.3.1.   FIRST METHOD: MAXWELL RELATIONS

The first method is in-line with the approach for developing thermodynamic tables presented in [26]. In this approach both Clapeyron and Maxwell relations are used with necessary numerical differentiation and integration. This approach requires virial equation of state (for the superheated region) and ideal specific heat capacity ($C_p{}^0$) for R245fa.

The properties in the saturated vapour line of the dome are already computed as discussed in Section 2.1. The approach presented here basically uses these values as reference to 'march' towards the superheated state of interest. Therefore, as given in [26], change in enthalpy/entropy (considering two points 1 and 2) can be calculated using;

$$\Delta h = h_2 - h_1 = \int_{T1}^{T2} C_p \ dT \ + \int_{P1}^{P2} \left[v - T \left(\frac{\partial v}{\partial T} \right)_P \right] dP \tag{6}$$

$$\Delta s = s_2 - s_1 = \int_{T1}^{T2} \frac{C_p}{T} \ dT \ - \int_{P1}^{P2} \left[\left(\frac{\partial v}{\partial T} \right)_P \right] dP \tag{7}$$

where both Δh and Δs account for enthalpy and entropy changes respectively as a result of both pressure and temperature change simultaneously.

As illustrated in [27], the change in enthalpy from "state 1" to "state 2" can be obtained by marching from 1 through A and B to 2 as seen in Figure 4. Pressure P_a is an arbitrary pressure which will be selected low enough so as to make both states A and B fall into the region where the ideal gas approximation is valid. Enthalpy difference between 1-A is by pressure change (P_1-P_a) only, from A-B is by the temperature change and then B-2 is again by change in pressure.

In this approach, since P_a is selected as stated above, then C_p (specific heat capacity) relation to use becomes the $C_p{}^0$ which is valid for the ideal gas region, the advantage is that $C_p{}^0$ can solely be defined in terms of temperature. It replaces C_p which is a function of both pressure and temperature in the superheated region. It follows that in the gaseous region,
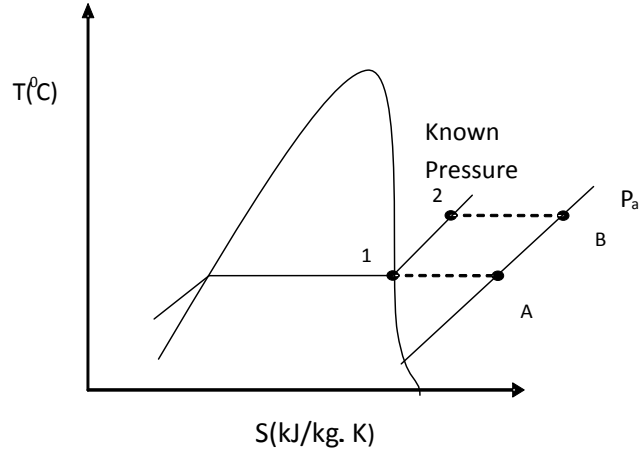
Figure 4: Superheated property calculation by integration.

the derivative terms in both Equations (6) and (7)) can be evaluated from the equation of state in the gaseous region. According to the study in [22], the Virial equation of state in the gaseous/superheated region is of the form;

$$P = MRT\rho.(1 + B\rho + C\rho^2) \qquad (8)$$

where R in the equation is universal gas constant = 8.31451 J/K.mol, M is molecular mass of R245fa = 134.05 kg/kmol.

B and C are functions of temperature T given as;

$$B = \sum_{n=0}^{4} B_i T^n \qquad\qquad C = \sum_{n=0}^{4} C_i T^{-n}$$

$C_p{}^0$ was also given in the form;

$$C_p{}^0 = A_0 + A_1 T + A_2 T^2 \qquad (9)$$

Using the same regression approach previously mentioned, the constants in Equations (8) are (9) were obtained and can be presented in Table 5. $C_p{}^0$ values used for the regression were carefully selected to be in the region were ideal gas was valid.

In conclusion, once these constants are defined, Equations (6) and (7)) can be easily solved each for one unknown parameter. In accounting for change owing to pressure difference in Equations (6) and (7)), the derivative $(\partial v/\partial T)$ was solved by implementing a finite difference code since the equation of state was known, while the integrals where numerically solved in the model by Simpsons 1/3$^{\text{rd}}$ rule. Since $C_p{}^0$ is a quadratic function of temperature, its

11

Table 5: Regression coefficients of Equations (8) and (9).

i	A	B	C
0	0.038954	-0.00377	4.59×10^{-7}
1	0.003728	0.00000	-0.00494
2	3.2×10^{-6}	-5.3×10^{-8}	0.00000
3	-	0.00000	-2.4×10^{-8}
4	-	-5.08×10^{-13}	-
R^2	0.9999	0.9864 (for Equation (8))	

integral can be evaluated analytically to be included in the model. For both enthalpy and entropy changes by temperature alone (as between states A-B in Figure 4);

$$h_B - h_A = A_0(T_B - T_A) + \frac{A_1\left(T_B{}^2 - T_A{}^2\right)}{2} + \frac{A_2\left(T_B{}^3 - T_A{}^3\right)}{3} \tag{10}$$

$$s_B - s_A = A_0 \, ln(T_B/T_A) + A_1(T_B - T_A) + \frac{A_2\left(T_B{}^2 - T_A{}^2\right)}{2} \tag{11}$$

where T is expressed in Kelvin.

2.3.2. SECOND METHOD: NON-LINEAR REGRESSION

This is a method proposed in [25], where two variable non-linear regression models was used to define specific enthalpy, specific entropy and density for both R600 and R600a in the superheated region of the form;

$$z = a_0 + a_1 x + a_2 y + a_3 x + a_4 y^2 + a_5 xy \tag{12}$$

where a_0 to a_5 are constants.

Three cases were devised;

(i) Case 1: h as a function of T and P.
(ii) Case 2: h as a function of s and P.
(iii) Case 3: ρ (density) as a function of P and h.

$$h(T, P) = a_0 + a_1 T + a_2 P + a_3 T^2 + a_4 P^2 + a_5 TP \tag{13}$$

$$h(s, P) = a_0 + a_1 s + a_2 P + a_3 s^2 + a_4 P^2 + a_5 sP \tag{14}$$

$$\rho(P, h) = a_0 + a_1 \ln(h) + a_2 P + a_3 (\ln(h))^2 + a_4 P^2 + a_5 \, \ln(h) \, P \tag{15}$$

where T is in Kelvin, P is in kPa, h in kJ/kg and density is in kg/m^3.

Depending on the property of interest, if two of the variables in Equation (12) are known, the third could be determined. Constants $a_0 - a_5$ are to be determined in pressure ranges. Here, pressure ranges used for the regression were in steps of 200 kPa as in [25]. Regression results for the three cases can be tabulated in Table 6.

Table 6: Regression coefficients for superheated region of R245fa.

P (kPa)		a_0	a_1	a_2	a_3	a_4	a_5	R^2
100-300	Case1	5.85 E -3	9.63 E -1	-1.44 E -1	-7.00E -5	5.71 E - 5	2.86 E -4	1.0000
	Case2	6.72 E +1	8.61 E +1	1.05 E -1	1.11E +2	-2.40 E -4	9.10 E -2	1.0000
	Case3	-5.60 E -4	1.02 E -1	1.65 E -3	1.94E -5	-3.50 E -7	-1.87 E -4	0.9999
300-500	Case1	5.16 E -3	9.38 E -1	-1.01 E -1	-1.60E -5	9.25 E -7	2.33 E -4	1.0000
	Case2	6.72 E +1	8.61 E +1	8.25 E -2	1.11E +2	-1.50 E -4	8.33 E -2	0.9999
	Case3	-7.20 E -4	1.16 E -1	-9.19 E -3	1.79E -5	4.37 E -05	-2.39 E -4	0.9999
500-700	Case1	5.48 E -3	9.32 E -1	-9.57 E -2	-1.60E -5	-7.60 E -6	2.41 E -4	1.0000
	Case2	6.72 E +1	8.61 E +1	6.28 E -2	1.11E +2	-8.70 E -5	7.36 E -2	0.9998
	Case3	-4.50 E -4	1.25 E -1	-2.08 E -2	9.77E -6	6.89 E -5	-2.50 E -4	0.9999
700-900	Case1	5.15 E -3	9.37 E -1	-9.79 E -2	-1.40E -5	-3.20 E -6	2.30 E -4	1.0000
	Case2	6.72 E +1	8.61 E +1	4.92 E -2	1.11E +2	-5.90 E -5	6.73 E -2	0.9999
	Case3	-7.60 E -4	1.52 E -1	-7.98 E -2	6.20E -6	2.34 E -4	-3.16 E -4	0.9998
900-1100	Case1	5.48 E -3	9.32 E -1	-9.57 E -2	-1.61E -5	-7.28 E -6	2.41 E -4	0.9999
	Case2	6.72 E +1	8.61 E +1	4.68 E -2	1.11E +2	-4.25 E -5	5.56 E -2	0.9998
	Case3	-2.20 E -4	1.29 E -1	-1.70 E -2	1.83E -5	1.45 E -4	-3.17 E -4	0.9998
1100-1300	Case1	5.15 E -3	9.37 E -1	-9.79 E -2	-1.00E -4	-1.30 E- 5	2.89 E -4	1.0000
	Case2	6.72 E +1	8.61 E +1	3.83 E -2	1.11E +2	-3.30 E- 5	5.33 E -2	0.9999
	Case3	-3.10 E -4	1.40 E -1	-3.56 E-2	2.50E -5	3.13 E -4	-4.03 E -4	0.9994

Note that when solving case 1 for *T* when both *h* and *P* are known, it was hinted in [25], the minimum root of the resulting quadratic equation to be used.

Other properties such as viscosity and thermal conductivity in the superheated state is evaluated using their respective values in gas at atmospheric pressure [23] followed by a correction step to the required pressure. Following regression on the reported experimental results on gaseous R345fa, thermal conductivity is defined in [23] with the following correlation:

$$k = k_{atm} + \sum_{i=0}^{2} \sum_{j=1}^{2} E_{ij} T^i [(P - 100).10^{-3}]^j \qquad (16)$$

where k_{atm} (at atmospheric pressure of 100kPa) can be defined as a function of temperature given by

$$k_{atm} = \sum_{i=0}^{3} E_i T^i \qquad (17)$$

Subsequently, the expression for viscosity in the gaseous region was also given in [23] as

$$\mu = \mu_{atm} + \sum_{i=0}^{4} D_i \rho^i \qquad (18)$$

Similarly,

$$\mu_{atm} = \sum_{i=0}^{3} D_{0i} T^i \qquad (19)$$

Due to the complicated form of Equation (16), it was observed that regression of its constants required not only a computationally demanding solver and but they are prone to errors. The following form of the equation helps in reducing the computational time of the regression with better accuracy was devised and proposed as follows;

$$k = k_{atm} + F_1 + F_2(P - 100).10^{-3} + F_3 T + F_4 T(P - 100).10^{-3} \qquad (20)$$

The values of the constants (D_i, D_{0i}, E_i, F_i) in Equations (17)-(20) as regressed from the tables can be seen in Table 7, along with error for a test state where T=30 ^{0}C and P=150 kPa. In these equations, T, P and ρ are to be input in Kelvin, kPa and kg/m^3 respectively.

Table 7: Regression constants for viscosity and thermal conductivity.

i	For μ (10^{-6}Pa.s)		For k (W/m^2.K)	
	D_i	D_{0i}	E_i	F_i
0	-6.91 E -08	-2.69 E +00	-1.36 E -02	-
1	-2.18 E -06	5.09 E -02	1.00 E -04	5.22 E -03
2	-5.37 E -05	-3.00 E -05	-2.00 E -07	2.07 E -03
3	1.42 E -05	1.00 E -08	3.00 E -10	7.45 E -06
4	-1.71 E -07	-	-	-1.73 E -06
%error for test state	$\left\|\frac{9.91-10.45}{10.45}\right\|$ = <u>5.2%</u>.		$\left\|\frac{0.0142-0.0143}{0.0143}\right\|$ = <u>0.7%</u>.	

CHAPTER 3

3. NUMERICAL MODEL OF THE ORGANIC RANKINE CYCLE

The numerical model of the ORC developed in this study is a synthesis of evaporator, condenser, pump and expander models representing the major components of a typical ORC. Each of these will be discussed in subsequent sections of this chapter.

3.1. The Evaporator

Evaporator is one of the key components of the ORC as it receives the energy from the heat source. Considering the time variation of the solar heat source, the transient behaviour of the evaporator is modelled. The evaporator model is formed using a typical counter-flow concentric tube heat exchanger. The solar irradiation is converted into heat by parabolic through collectors and transferred to the ORC unit's evaporator via compressed liquid water. The evaporator's task is to transfer this energy to the sub-cooled refrigerant and to bring it to the vapour state.

A finite volume discretization approach for the heat exchanger is used to simulate the behaviour of the evaporator. Figure 5 illustrates the representation of the heat exchanger cross section for the approach.
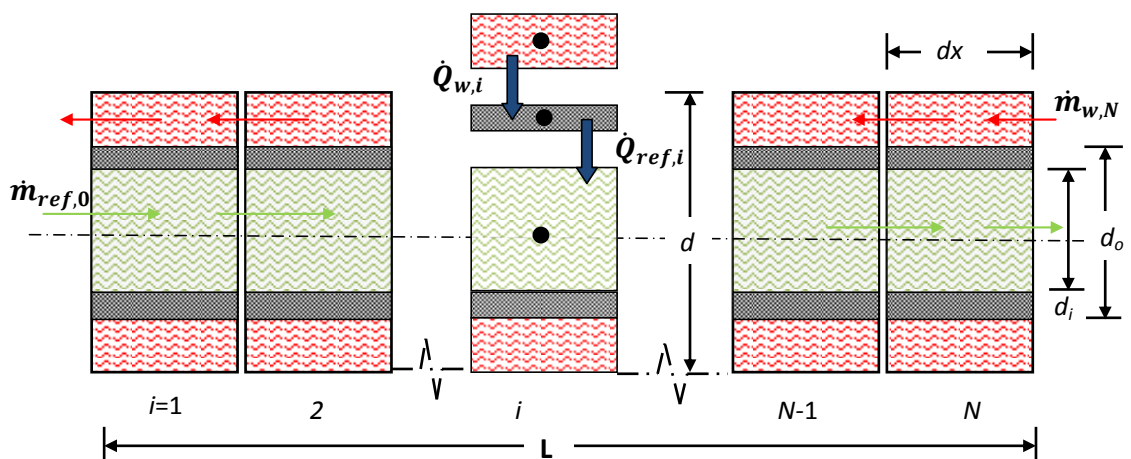

Figure 5: Finite volume representation of the heat exchanger.

The evaporator model considers mass and energy balance equations for a uniform flow. The momentum equation is not considered as the pressure drop along the evaporator is neglected. Figure 5 represents the simplified evaporator's geometry with 1-D finite volume discretization. Then, for each ith control volume, mass conservation equation written for the refrigerant gives;

$$\frac{d\dot{m}_{cv}}{dt} = \dot{m}_{ref,i-1/2} - \dot{m}_{ref,i+1/2} = V_{ref}\frac{\partial \rho_{ref,i}}{\partial t} \tag{21}$$

The energy equation for the refrigerant can be established thus;

$$\frac{dE_{ref,i}}{dt} = V_{ref}\frac{d(\rho_{ref,i}h_{ref,i} - P_{ref})}{dt} \tag{22}$$
$$= q_{ref,i} + \dot{m}_{ref,i-1/2}h_{ref,i-1/2} - \dot{m}_{ref,i+1/2}h_{ref,i+1/2}$$

$$V_{ref}h_{ref,i}\frac{\partial \rho_{ref,i}}{\partial t} + V_{ref}\rho_{ref,i}\frac{\partial h_{ref,i}}{\partial t} \tag{23}$$
$$= \dot{Q}_{ref,i} + \dot{m}_{ref,i-1/2}h_{ref,i-1/2} - \dot{m}_{ref,i+1/2}h_{ref,i+1/2}$$

Combining equation (21) and (23) yields

$$V_{ref}\rho_{ref,i}\frac{\partial h_{ref,i}}{\partial t} = \dot{Q}_{ref,i} + \dot{m}_{ref,i-1/2}(h_{ref,i-1/2} - h_{ref,i}) - \dot{m}_{ref,i}(h_{ref,i+1/2} \tag{24}$$
$$- h_{ref,i})$$

The energy equation for the pipe is as follows;

$$\frac{\partial E_{p,i}}{\partial t} = \rho_p V_p C_{p,p}\frac{\partial T_{p,i}}{\partial t} = \dot{Q}_{w,i} - \dot{Q}_{ref,i} + \dot{Q}_{cond\,p,i} \tag{25}$$

Also for the water;

$$\frac{\partial E_{w,i}}{\partial t} = \rho_w V_w C_{p,w}\frac{\partial T_{p,i}}{\partial t} = \dot{m}_w C_{p,w}(T_{w,i+1} - T_{w,i}) - \dot{Q}_{w,i} \tag{26}$$

Following the energy equations, assumptions made include;

  a. The outer shell with diameter d is strongly insulated and heat transfer and heat transfer area is between flowing hot-water and pipe to the refrigerant.
  b. Solid pipe's material properties are assumed to be constant.

c. From the known operation of the solar collectors, hot-water (inlet and exit) is always at compressed liquid state therefore constant mass flow rate is assumed for water.

Equations (21) - (26) are to be solved with given inflow state conditions (mass flow rate, temperatures and enthalpy) and yield time dependent state conditions at the exit of the evaporator. To summarize, the intended model is represented in the model-block of Figure 6, which shows the inputs of the model to provide required results.
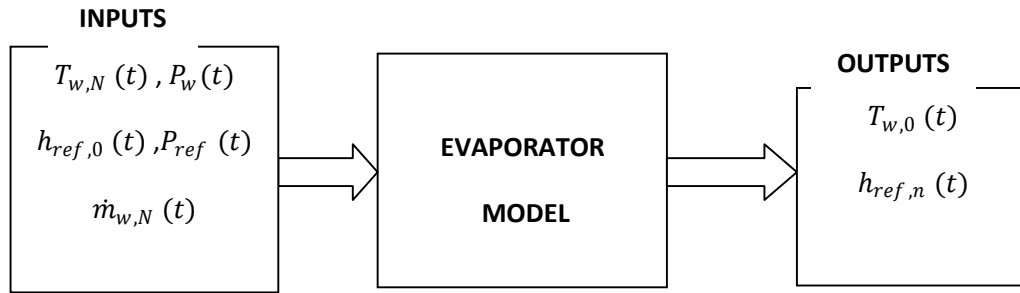
INPUTS

$T_{w,N}(t), P_w(t)$

$h_{ref,0}(t), P_{ref}(t)$

$\dot{m}_{w,N}(t)$

EVAPORATOR

MODEL

OUTPUTS

$T_{w,0}(t)$

$h_{ref,n}(t)$

Figure 6: Block diagram of evaporator model.

3.1.1. NUMERICAL MODEL

The transient term on the left hand side of Equations (21)-(26) can be integrated using either (i) the explicit method (where all terms are written as previous/known time) or (ii) implicit method (when all terms are written for the current/unknown time) with specific advantages and disadvantages for each method as explained in [27].

A. The Explicit approach

The explicit method is easier to program as solutions of the Equations (21)-(26) could be obtained 'marching' from the inlet node to the exit. After neglecting the $V_{ref}(\partial P_{ref})/\partial t$ term in Equation (22) and considering first order upwind for convective terms, Equations (27)-(29) are solved in the order presented to obtain enthalpies and temperatures at the new time step.

Equation (27) is solved first to obtain the enthalpy variation of R245fa. When needed, all other state variables throughout the pipe can be obtained using enthalpy and pressure.

$$h_{ref,i}{}^{t+1} = h_{ref,i}{}^t + \Delta t \left[\frac{AH_{ref,i}{}^t\left(T_{p,i}{}^t - T_{ref,i}{}^t\right) + \dot{m}_{ref,i}{}^t\left(h_{ref,i-1}{}^t - h_{ref,i}{}^t\right)}{V_{ref}\rho_{ref,i}{}^t} \right] \qquad (27)$$

17

Equation (27) is then followed by Equation (28) to solve temperature variation of the pipe.

$$T_{p,i}{}^{t+1} = T_{p,i}{}^{t} + \Delta t \left[\frac{H_w{}^{t}A\left(T_{w,i}{}^{t} - T_{p,i}{}^{t}\right) + AH_{ref,i}{}^{t}\left(T_{ref,i}{}^{t} - T_{p,i}{}^{t}\right) + \dot{Q}_{condp,i}{}^{t+1}}{V_p \rho_p C_p} \right] \quad (28)$$

Finally, Equation (29) is solved to obtain the temperature variation of water stream at the pipe annulus.

$$T_{w,i}{}^{t+1} = T_{w,i}{}^{t} + \Delta t \left[\frac{\dot{m}_w{}^{t}C_{p,w}{}^{t}\left(T_{w,i+1}{}^{t} - T_{w,i}{}^{t}\right) + H_w{}^{t}A\left(T_{p,i}{}^{t+1} - T_{w,i}{}^{t}\right)}{V_w \rho_{w,i}{}^{t} C_{p,w}{}^{t}} \right] \quad (29)$$

where, A can be defined as $\pi d\, \Delta x$. The conduction heat transfer term in the Equation (28) is expressed as follows;

$$\dot{Q}_{condp,i}{}^{t+1} = \frac{k\pi(do^2 - di^2)}{4\,\Delta x}\left(2T_{p,i}{}^{t+1} - T_{p,i-1}{}^{t+1} - T_{p,i+1}{}^{t+1}\right) \quad (30)$$

The major limitation of this approach arises from the stability criterion. Solutions to the above Equations (27)-(29) would be inaccurate if the simulation becomes unstable when a certain allowable Δt is exceeded. An estimate of the maximum allowable Δt value must be made in order to ensure suitable solution flow. Due to the parabolic nature of the pipe heat equation, stability of its solution could be guaranteed by using a *backward Euler* approach, therefore It should be observed that the equation for the pipe ((28)), is already implicitly represented.

The approach to calculate this value follows from the fact that the coefficients of the *i*th value of the variable of interest ($h_{ref,i}{}^{t}$ & $T_{w,i}{}^{t}$) on the RHS of Equations (27) and (29) respectively must add-up to be greater than equal to zero. It then follows from equations (27) that;

$$1 + \Delta t \left(\frac{AH_{ref,i}{}^{t}}{V_{ref}\rho_{ref,i}{}^{t}C_{p,ref}{}^{t}} - \frac{\dot{m}_{ref,i}{}^{t}}{V_{ref}\rho_{ref,i}{}^{t}} \right) \geq 0 \quad (31)$$

Therefore;

$$\Delta t \leq \frac{-V_{ref}\rho_{ref,i}{}^{t}C_{p,ref}{}^{t}}{AH_{ref,i}{}^{t} - \dot{m}_{ref,i}{}^{t}C_{p,ref}{}^{t}} \quad (32)$$

This time constant could be evaluated at the initial time and used throughout the duration of problem solution for convenience. $AH_{ref,i}{}^{t}$ is expected to be less than $\dot{m}_{ref,i}{}^{t}C_{p,ref}{}^{t}$ for this

equation to be valid, therefore if the $AH_{ref,i}{}^t$ term from the heat transfer part of Equation (27) were to be neglected, the resulting Δt would be less than that calculated from Equation (32). This gives;

$$\Delta t \ \leq \ \frac{V_{ref}\rho_{ref,i}{}^t}{\dot{m}_{ref,i}{}^t} \tag{33}$$

Also for water in Equation (29);

$$1 - \Delta t \ \left(\frac{AH_w{}^t + \dot{m}_w{}^t C_{p,w}{}^t}{V_{ref}\rho_w{}^t C_{p,w}{}^t} \right) \geq 0 \tag{34}$$

This gives;

$$\Delta t \ \leq \ \frac{V_{ref}\rho_w{}^t C_{p,w}{}^t}{AH_w{}^t + \dot{m}_w{}^t C_{p,w}{}^t} \tag{35}$$

Equations (33) and (35) represent the limits for the allowed time stepping and the minimum of the two will be selected for the whole simulation.

B.   The Implicit approach

The restriction for the time stepping imposed by the explicit approach could be very severe (around tenths of seconds) resulting in more computation time and becomes unpractical for longer time operations of the heat exchanger (E.g. daily simulation). Implicit approach can remove this limitation. For the refrigerant, Equation (27) can be modified to give;

$$h_{ref,i}{}^{t+1} = \ h_{ref,i}{}^t + \mathrm{B} \left(q_{ref,i}{}^t + \ \dot{m}_{ref,i-1}{}^{t+1} h_{ref,i-1}{}^{t+1} - \ \dot{m}_{ref,i}{}^{t+1} h_{ref,i}{}^{t+1} \right) \tag{36}$$

where $\mathrm{B} = \ \Delta t / V_{ref}\rho_{ref,i}{}^t$.

For each time step, $h_{ref,i}$ can be obtained by solving an (N by N) system of equation of the form (recall that $h_{r,ef0}$ is known);

$$[\mathrm{X}] \left[h_{ref,i} \right] = \ [\mathrm{Y}] \tag{37}$$

where [X] is a lower triangular matrix with only coefficients on the main diagonal and that directly below, and [Y] would be the (N by 1) matrix formed from the known values at previous time step.

Substituting the all heat transfer terms for the pipe, Equation (28) gives;

$$T_{p,i}^{t+1} = T_{p,i}^{t} + b\left(q_{w,i}^{t} - q_{r,i}^{t}\right) - ab\left(2T_{p,i}^{t+1} - T_{p,i-1}^{t+1} - T_{p,i+1}^{t+1}\right) \qquad (38)$$

where $b = \Delta t/V_p \rho_p$ and $a = k\pi(do^2 - di^2)/4dx$.

Similarly, this representation would give an (N by N) system of equations for each time step where the [X] would be a Topelitz matrix considering the coefficients of three terms (*i-1, i* and *i+1*) appear.

For water, considering the inlet water temperature $(T_{w,N+1}^{t})$ as known, the implicit representation can be expressed thus;

$$T_{w,i}^{t+1} = T_{w,i}^{t} + R\left(T_{w,i+1}^{t+1} - T_{w,i}^{t+1}\right) - S\,q_{w,i}^{t} \qquad (39)$$

where $R = \Delta t \dot{m}_w^{t}/V_w \rho_w^{t}$ and $S = \Delta t/V_p \rho_w^{t} C_{p,w}^{t}$.

The [X] for water would be an upper triangular matrix with only non-zero coefficients in the main diagonal and the diagonal just above it. The [Y] would be the matrix of the known values at previous time step as with the case for refrigerant and pipe.

C. The solution approach

The solution approach which was devised and used includes a blend of the implicit and explicit representations. This approach suggests solving only the equation for the pipe implicitly by following the representation in Equation (38). For all other equations (for water and refrigerant) the same process as in the explicit approach is adopted as it was discovered that a purely implicit approach (for all equations) give similar values for a group of nodes in the descretization. A solution algorithm summarized for this approach (given known inlet conditions) can be described in the following steps;

    a. Solve Equation (29) and (27) for the water and refrigerant respectively marching from inlet to exit node using previous $T_{p,i}$ values.

    b. An explicit solution for the pipe; updating $T_{p,i}$ values for the next time step by establishing and solving the system of simultaneous equations.

3.1.2. HEAT TRANSFER COEFFICIENTS

The established model would only be valid if it can adequately predict the respective heat transfer coefficients in each discrete node for the required total heat transfer area. As prescribed by [28] and previously stated assumptions the convective heat transfer coefficient

H_w between the water and pipe will not vary with location but only with time, while that between the pipe and refrigerant H_{ref} will vary with both time and location as its physical properties change. Therefore, the thermodynamic state in each node will be the strong determinant of H_{ref}.

A. Single phase heat transfer coefficient

For states with fluid in single phase, as with the water and both sub cooled and gaseous states of the refrigerant, the convective heat transfer coefficients can be obtained using suitable Nusselt number correlations under constant heat flux assumption given in [29].

For laminar flow (characterised by $Re < 2300$) and fully developed;

$$Nu = \frac{H d_h}{k} = 4.36 \tag{40}$$

which gives heat transfer coefficient as $H = \frac{4.36\, k}{d_h}$

Where H is the required fluid's heat transfer coefficient, k is its thermal conductivity and d_h represents the hydraulic diameter of the flow cross section.

For the water (in the annulus), d_h for heat transfer calculations is given in [28] as;

$$d_h = \frac{(d^2 - do^2)}{do} \tag{41}$$

while $d_h = d_i$ for the refrigerant in the tube (as seen in Figure 5).

For fully turbulent flow (Re>4000), the Gneilinski equation was used, which is given as;

$$Nu = \frac{(f/8)(Re - 1000)Pr}{1 + 12.7(f/8)^{0.2}(Pr^{2/3} - 1)} \tag{42}$$

$$\text{Where } f = (0.79 \ln Re - 1.64)^{-2} \tag{43}$$

Reynolds number, *Re,* can be written in terms of the mass flow rate as;

$$Re = \frac{\dot{m} d_h}{A_c \mu} \tag{44}$$

B. Two-phase heat transfer coefficient

When boiling of the refrigerant takes place it is in two phase (saturated mixture). To evaluate the heat transfer coefficient for the fluid in this region, Chen-type correlations have been popularly used in literature as also seen in [30]. The Chen correlation considers both vaporization and nucleate boiling taking place.

In a study by Sun & Mishima [31] , thirteen prediction models for flow boiling heat transfer in mini-channels were evaluated and compared. They concluded that the Chen-type correlations were not as suitable for mini-channels as compared to those with a Weber number term, such as the Lazarek–Black and Kew–Cornwell correlations which were proven to be the most suitable. It was also suggested in the study that none of the models could as yet lay exclusive claim to being the universal model for calculating flow boiling heat transfer coefficient. Therefore for simplicity and faster computation, the Kenning and Cooper correlation as presented in [31] was used in this work.

In the Chen-type correlations, the two-phase Nusselt number was presented as an addition of that of the single phase and that of Nucleate boiling, however the Kenning and Cooper correlation gives;

$$Nu_b = \left(1 + 1.8\, X_{tt}^{-0.87}\right) Nu_{sp} \tag{45}$$

where Nu_{sp} is the single phase Nusselt number which is defined by;

$$Nu_{sp} = 0.023\, Re_l^{0.8}\, Pr_l^{0.4} \qquad \text{(Dittus-Boelter correlation)} \tag{46}$$

where X_{tt} is known as the Martinelli factor expressed as;

$$X_{tt} = \left(\frac{1-x}{x}\right)^{0.9} \left(\frac{\rho_v}{\rho_l}\right)^{0.5} \left(\frac{\mu_l}{\mu_v}\right)^{0.1} \tag{47}$$

Re_l is the Reynolds number for the liquid in the mixture and can be expressed as;

$$Re_l = \frac{\dot{m}\, d_h (1-x)}{A_{c,ref}\mu_l} \tag{48}$$

Following Equations (45)-(48), the heat transfer coefficient is calculated by,

$$H_b = \frac{Nu_b k_l}{d_h} \tag{49}$$

It was clearly seen in [31] that the Kenning and Cooper correlation predicts lower nodal heat transfer coefficients than the Chen correlation. This comparison between the two correlations is also illustrated in Figure 7 for the test case presented in [30] where water boils at atmospheric pressure in a 0.02 m diameter tube with a 0.1 kg/s flow when pipe temperature kept constant at 120 ^{0}C. It can be observed from the figure that; in the vapour quality test range of 0.15-0.75, the Chen correlation used by Vaja [30] predicts lower heat transfer coefficient than both Chen correlation (Chen orig.) and Kenning & Cooper (K&C) correlations as presented in [31].
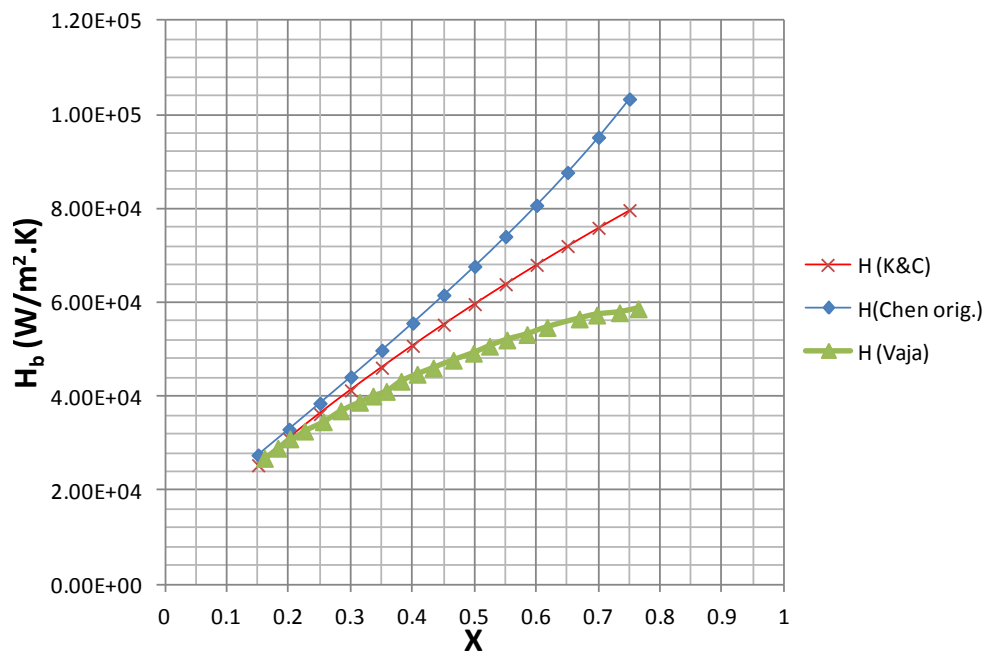
Figure 7: Comparison of boiling heat transfer coefficient correlations for test case.

It is worthy of note that there is usually an order of magnitude difference in the values of H_{ref} in single phase and that in the two-phase region as mentioned in [30]. This results in a jump in the value of H_{ref} in its transition from single phase which would cause stability problems in the model. This jump was described as a direct consequence of the questionable accuracy of the two-phase correlations in the regions where $0 < x < 0.1$ and $0.9 < x < 1$. To mitigate any stability problems that could arise from this situation, the use of dumping coefficients which would help smoothen the H_{ref} curve were suggested. In this work, dumping coefficients would be used in the regions of vapour quality below 0.15 and above 0.75 as seen in [31]. The dumping coefficients simply linearizes the predicted two-phase

heat transfer between the mentioned limiting cases and the adjacent H_{ref} values at saturated liquid and saturated vapour ($x = 0$ and $x = 1$) to avoid the jump.
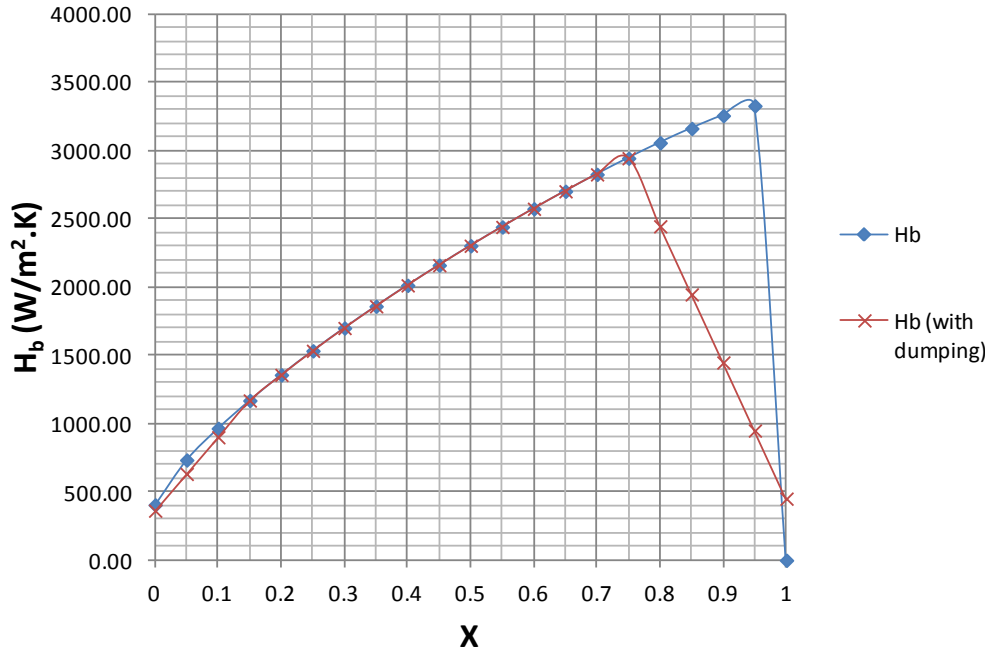

Figure 8: Variation of boiling heat transfer coefficient with vapour fraction.

Figure 8 illustrates the benefit of using the two-phase correlations in conjunction with dumping coefficients to smoothen the transition of H_{ref} for a test case using the Kenning and Cooper correlation if R245fa boils at 300kPa where d_i = 8mm and $\dot{m}_{ref}$ = 0.01kg/s at a constant pipe temperature of 81^0C. In this way, the curve is continuous, joining the calculated values from the single phase correlations for $x = 0$ and $x = 1$ (saturated liquid and vapour) instead of zeros that may arise from the two-phase correlations near $x = 0$ and $x = 1$.

With all the necessary equations developed and programmed in MATLAB, Important steps to take before a solution can be reached include;

    a. Selecting proper boundary conditions (at the inlet and exit nodes).

    b. Enforcement of initial distribution of the temperatures, enthalpy and flow rates across each node to 'kick-start' the solution.

c. This was done easily by assuming constant values for the initial time step. i.e. $T_{w,N}{}^{0} = T_{w,i}{}^{0}$, $h_{ref,0}{}^{0} = h_{ref,i}{}^{0}$, $\dot{m}_{ref,0}{}^{0} = \dot{m}_{ref,i}{}^{0}$ and $T_{p,i}{}^{0} = 0.5 \times (T_{ref,i}{}^{0} + T_{w,i}{}^{0})$

3.1.3. EVAPORATOR SIMULATION RESULTS

The heat exchanger (as either evaporator or condenser) in the ORC unit that inspires this study are brazed plate heat exchanger type (shown in Figure 9). It differs in physical features (geometry) from the representation in Figure 5 as it is made a compact heat exchanger to reduce the size. Nevertheless it is also a counter-flow type, therefore a concentric tube analogy (similar to Figure 5) could be applied if the total heat transfer area by its mini-channels is obtained. The dimensions of its concentric tube approximation may not be realistic (in terms of manufacturing) but it should serve the purpose of the heat transfer investigation.
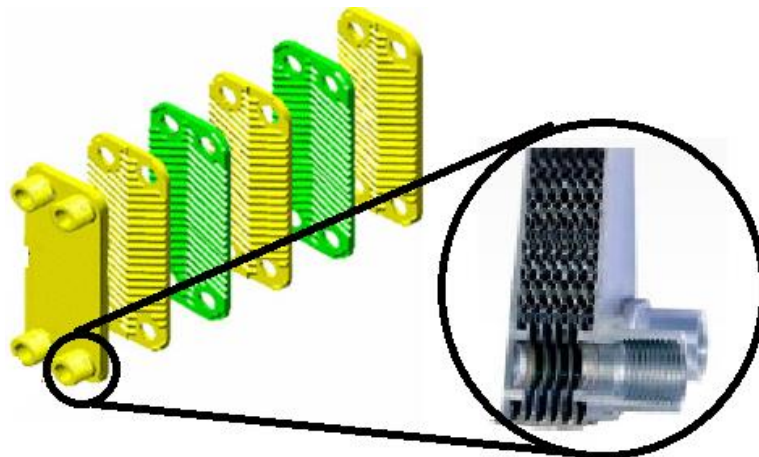
Figure 9: Brazed plate heat exchanger
Images from: http://www.kaori-taiwan.com/brazed-plate.html

The following graphs would show results for a test simulation to investigate the transition towards steady state given steady inlet conditions (constant with time) based on the model in Figure 5 with the dimensions of the concentric tube approximation. These theoretical dimensions presented in Table 8 would be maintained and used for the evaporator in the rest of this study.

The test simulation was run with hot water of 12 kg/s entering at 93^{0}C (atmospheric pressure) and inlet refrigerant was compressed liquid of temperature 25 ^{0}C and pressure

628.22 kPa (enthalpy ≈ 83.3 kJ/kg) with inlet mass flow rate of 1.5 kg/s. The simulation has 0.085 sec as time step (Δt) and does not account for any pressure drop of refrigerant, the resulting graphs was made to show the transition of the variables in each node i.e. each graph consists of 12 lines representing inlet, each ith-node and the outlet respectively. (for N = 10).

Table 8: Evaporator (theoretical) dimensions.

Parameter	Value	Parameter	Value
L	80.0000m	d	0.1235m
d_o	0.0686m	d_i	0.0656m

*Pipe material is stainless steel, A ≈ 18m^2.

Figure 10 shows the nodal variation of hot water temperature with time. It should be noted that the truncation of this simulation was based on the hot water temperature and the mass flow rate was kept constant. The MATLAB code was programmed to stop this simulation once the maximum hot water temperature difference experienced from one time step to the next becomes less than 0.0001^{0}C (i.e. achieved steady state). Therefore, it can be said that steadiness was achieved after about 295 sec.
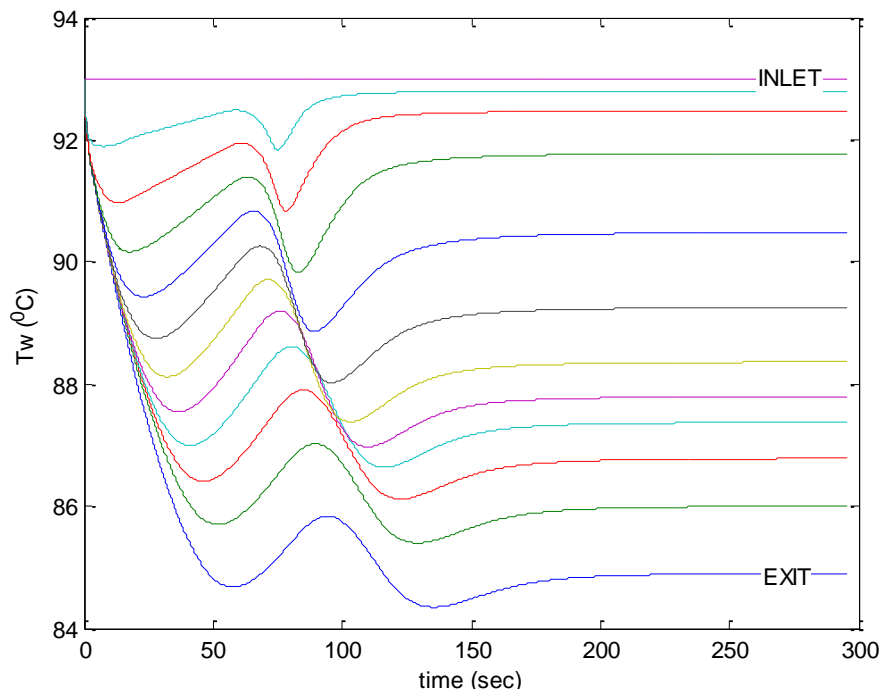
Figure 10: Variation of hot water temperature.

26
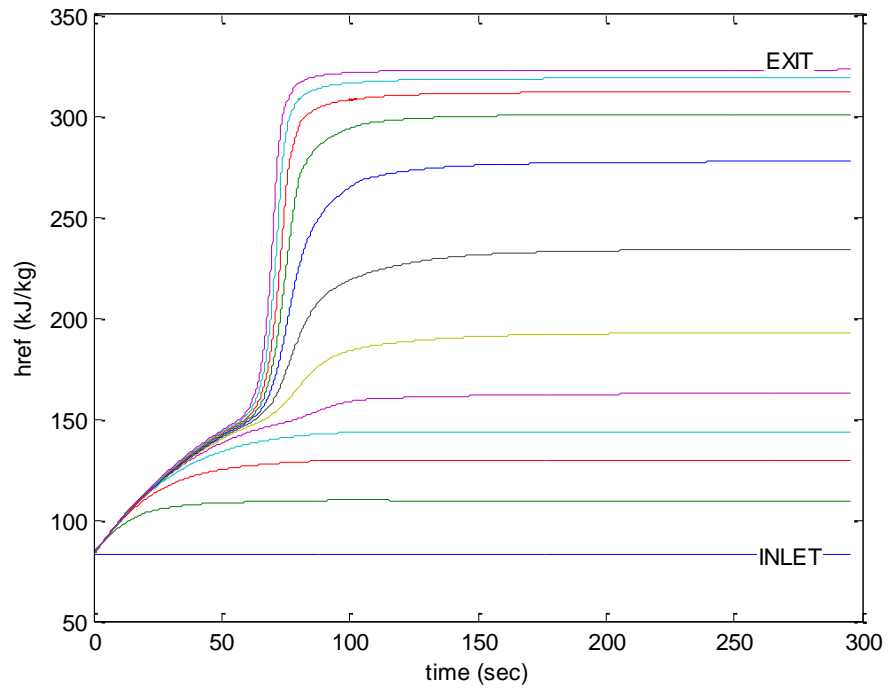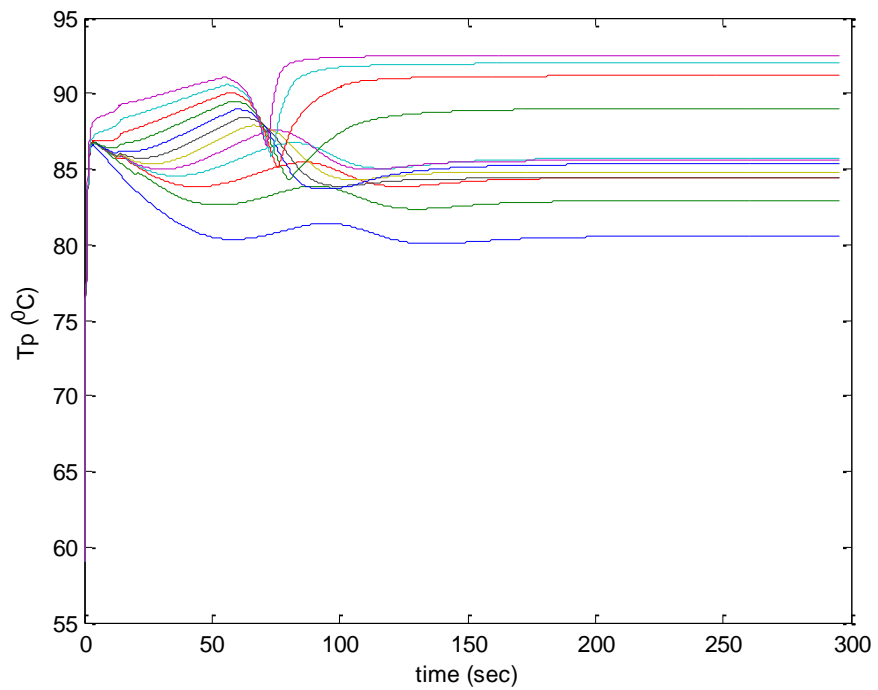
Figure 11: Variation of specific enthalpy of R245fa.

Figure 12: Temperature variation of solid pipe.

Specific enthalpy of the refrigerant for each node is shown in Figure 11. The refrigerant is shown to exit at 86.8693 ^{0}C as superheated vapour using the refrigerant saturated properties at the given pressure. The following graph of Figure 12 plots the nodal pipe temperature variation with time with initial conditions, $T_{p,i}{}^0 = 0.5 \times (T_{ref,i}{}^0 + T_{w,i}{}^0)$ as earlier mentioned.
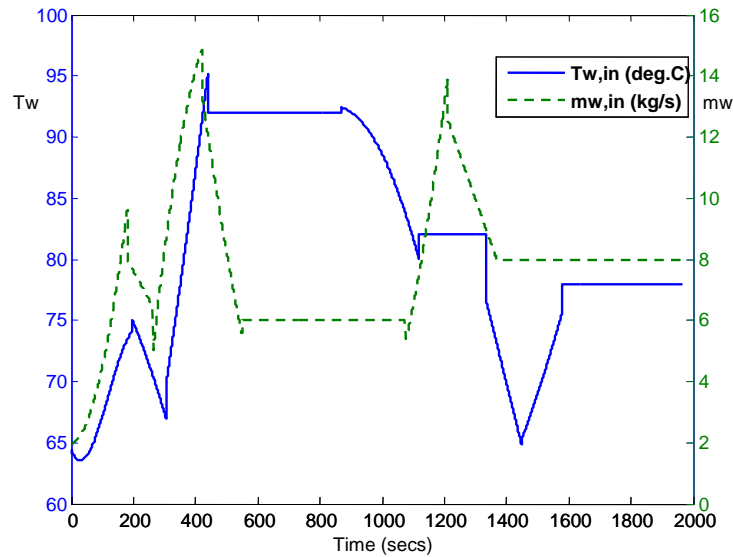

Figure 13: Variation of hot-water input parameters.

To aid a better visualization of the transient operation of the evaporator, a dynamic scenario where the available heat input to the system rapidly varies within a short time is presented. This situation is a usual case for ORCs in energy recovery applications in vehicles and other IC-engines like the investigation in [18]. In this test situation, inlet hot water temperature and mass flow rate profiles are shown in Figure 13.

The profile in Figure 13 was input to the evaporator model where the refrigerant is at 628.22 kPa,25 ^{0}C and flowing at a mass flow rate of 1.5 kg/s. The output of the model showing the variation of both T_{ref} and h_{ref} in time at the outlet is seen in Figure 14.

3.1.4. EFFECT OF NUMBER OF NODES

In an explicit approach, the stability limit defined by Equations (33) and (35) could be used to obtain the suitable time step to allocate for any simulation given the number of nodes (*N*) to be considered. Irrespective of the approach used, it is of general knowledge that greater *N* would yield more accurate results (as observed with any 'finite' method). However,
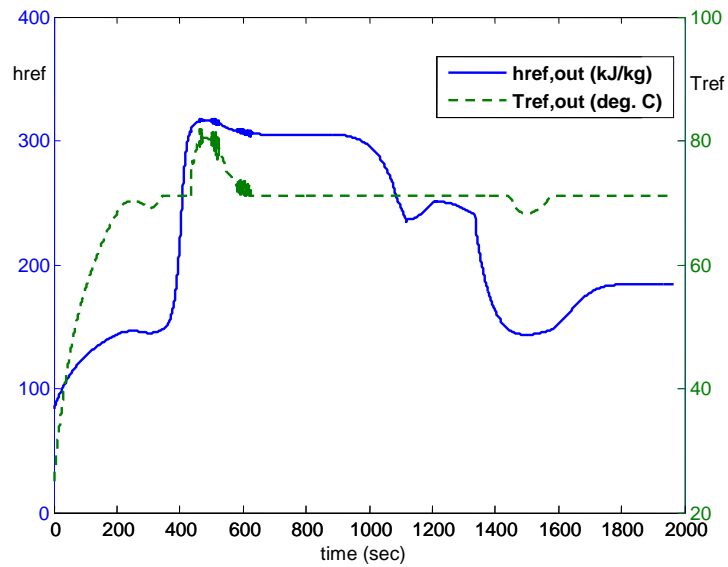
Figure 14: Variation of T_{ref} and h_{ref} at evaporator exit.

increasing *N* would increase the number of calculations to be done as allowable time step would also have to decrease, making simulation of lengthier events require more computational resources.
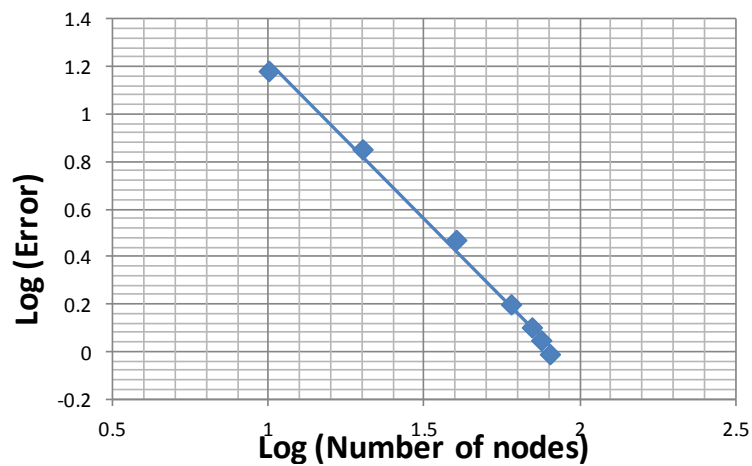

Figure 15: Effect of number of nodes on accuracy.

The deviation of results as *N* changes is depicted in Figure 15. Given that the sole purpose of a heat exchanger is to transfer heat from one fluid to the other, the graph uses constant fluid inlet conditions to compare the $\dot{Q}_{in}$ (after steady state is achieved) from different values

of N with an extreme case where N = 160. In this test case, 10 kg/s hot water enters the evaporator at 93 ^{0}C and atmospheric pressure with 0.75 kg/s R245fa inlet at 26.75 ^{0}C and 678.34 kPa.

Accuracy increases with increase in the value of N as expected, the converging trend seen in Figure 15 suggests it is unnecessary to expend more computational resources beyond a certain value of N. This results to selecting N = 60 as adequate for subsequent ORC simulations in the rest of this study.

3.1.5. STEADY STATE MODEL

Generally, steady state models are adequate for design purposes and transient models are required for dynamic simulations given unsteady inputs. At constant input conditions, it is necessary to be able to accurately estimate the heat exchanger output states without having to expend the computational resources of running a full transient simulation. Therefore this section discusses the resultant steady state model of the transient model discussed in the previous sections.

Energy equation across a heat exchanger can be expressed as in Equation (64).

$$\frac{\partial E}{\partial t} = \dot{Q}_{ev/co} + \dot{m}_{ref}\left(h_{ref,in} - h_{ref,out}\right) \tag{50}$$

At steady state, the term on the left hand side is zero (unlike when unsteady) and the heat transferred ($\dot{Q}_{ev/co}$) can be calculated using the enthalpy difference between the inlet and outlet states along with the mass flow rate. Since the exit state is not known in priori, effectiveness-NTU method is employed to estimate the heat energy transferred between water and refrigerant in the evaporator or condenser in terms of inlet temperatures.

$$\dot{Q}_{ev/co} = \varepsilon \dot{m}C_{p_{min}}\left(T_{hot,in} - T_{cold,in}\right) = \varepsilon \mathbb{C}_{min}\left(T_{hot,in} - T_{cold,in}\right) \tag{51}$$

where ε is a function of overall heat transfer coefficient (U), A, $C_{p,ref}$ and $C_{p,w}$.

In the present study, one of the fluids (refrigerant) is expected to undergo a change of state which is accompanied by a change of properties. As U is defined using Equation (52), it has been seen previously (in Figure 8) that the convective heat transfer coefficient on the refrigerant side would largely vary in magnitude as it undergoes state change. Due to these reasons, directly obtaining a single ε given only inlet temperatures proves elusive.

30

$$U \cong \frac{H_{ref} \, H_w}{H_{ref} + H_w} \tag{52}$$

In literature, these changes are taken into consideration by dividing the heat exchanger into three main segments on the provision that the fluid to be heated enters as compressed liquid and can exit at superheated/gaseous state. The approach used in this work draws inspiration from the work of Vargas et al. [32] where such an evaporator is assumed to be divided into three sub-segments; "*a preheater, a boiler and a superheater*" linked in series. The categorization accounts for the state transition as shown in Figure 16.
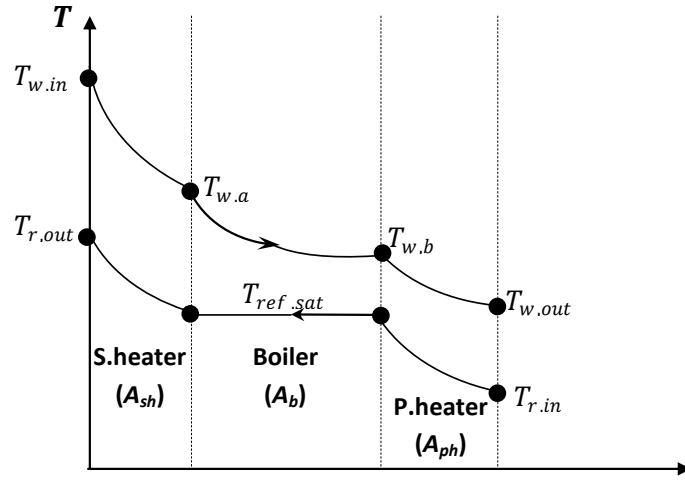
Figure 16: Representation of steady state model

A. Numerical model

Starting from the superheater, the effectiveness in that region is defined in terms of temperatures as;

$$\varepsilon_{sh} = \frac{\mathbb{C}_{ref,sh}(T_{ref,out} - T_{ref,sat})}{\mathbb{C}_{min,1}(T_{w,in} - T_{ref,sat})} = \frac{\mathbb{C}_{w,sh}(T_{w,in} - T_{w,a})}{\mathbb{C}_{min,1}(T_{w,in} - T_{ref,sat})} \tag{53}$$

where $\mathbb{C}_{min,1}$ is the minimum of $\mathbb{C}_{ref,sh}$ and $\mathbb{C}_{w,sh}$ (in the superheater segment), the above relations yields two equations;

$$T_{w,a} = T_{w,in} - \varepsilon_{sh} \frac{\mathbb{C}_{min,1}(T_{w,in} - T_{ref,sat})}{\mathbb{C}_{w,sh}} \tag{54}$$

31

$$T_{ref,out} = T_{ref,sat} + \varepsilon_{sh} \frac{\mathbb{C}_{min,1}(T_{w,in} - T_{ref,sat})}{\mathbb{C}_{r,sh}} \tag{55}$$

Two further equations can be similarly defined for the preheater where the minimum of $\mathbb{C}_{ref,ph}$ and $\mathbb{C}_{w,ph}$ is $\mathbb{C}_{min,2}$ as;

$$\varepsilon_{ph} = \frac{\mathbb{C}_{r,s}(T_{ref,sat} - T_{ref,in})}{\mathbb{C}_{min,2}(T_{w,b} - T_{ref,in})} \tag{56}$$

$$T_{w,out} = T_{w,b} - \varepsilon_{ph} \frac{\mathbb{C}_{min,2}(T_{w,b} - T_{ref,in})}{\mathbb{C}_{w,ph}} \tag{57}$$

For the boiler, the relationships are;

$$\varepsilon_b = \frac{T_{w,a} - T_{w,a}}{T_{w,a} - T_{ref,sat}} \tag{58}$$

$$T_{w,b} = T_{w,a} - \frac{\dot{m}_{ref}\, h_{lv}}{\mathbb{C}_{w,b}} \tag{59}$$

The relationships between effectiveness and NTU for such concentric tube counter flow heat exchanger configurations are obtained from [29]. Effectiveness as a function of NTU and $\mathbb{C}_{cr}$ (ratio of $\mathbb{C}_{min}$ to $\mathbb{C}_{max}$) is given as;

$$\varepsilon = \frac{1 - \exp(-(1 - \mathbb{C}_{cr}))}{1 - \mathbb{C}_{cr}\exp(-\text{NTU}\,(1 - \mathbb{C}_{cr}))} \tag{60}$$

A change of subject in Equation (60) gives NTU as a function of ε and $\mathbb{C}_{cr}$ defined by;

$$\text{NTU} = \frac{U\,A}{\mathbb{C}_{min}} = \frac{1}{\mathbb{C}_{cr} - 1}\, ln\left(\frac{\varepsilon - 1}{\varepsilon\mathbb{C}_{cr} - 1}\right) \tag{61}$$

When state change is involved (as in the boiler segment), Equation (61) simplifies to;

$$\text{NTU} = -ln(1 - \varepsilon) \tag{62}$$

Recalling the total heat transfer area has been segmented, which gives;

$$A = A_{sh} + A_b + A_{ph} \tag{63}$$

B. Solution approach

The solution approach of this study neglects changes in properties (with temperature) for hot water as the temperature transition range is quite narrow. Similar to the transient model developed, pressure drop across the heat exchanger is also neglected. Equations (54) to (61) are the set of simultaneous equations adequate to define all the unknowns. Given the nature of some of the equations, an iterative approach would be required to obtain the exit conditions of both refrigerant and hot water given known inlet conditions. The solution flow of the MATLAB code written to perform this task can be summarized as follows:

a. Estimating U_{sh} and U_{ph} using the values of H_{ref} and H_w at saturated vapour and saturated liquid states respectively, and U_b using average H_{ref} from integrating over the saturated mixture region.

b. Assume A_{sh} as a first guess.

c. Solve for ε_{sh} and $T_{w,a}$ using Equations (60) and (54) respectively.

d. Calculate the corresponding values of $T_{w,b}$ and ε_b with Equations (59) and (58) respectively and obtain a value for A_b with Equation (62).

e. Solve Equation (56) to obtain ε_{ph} and Equation (61) for the corresponding value of $A_{ph.}$

f. Use Equation (63) to check the assumed A_{sh}. If correct to the tolerance (0.005m^2), the iteration is truncated. Conversely, the steps are repeated using the new A_{sh} obtained until convergence.

g. Equations (55) and (57) are then used to calculate $T_{ref,out}$ and $T_{w,out}$ respectively.

NOTE: If after several iterations (20 in this study) the result does not converge or converges to give negative or complex final value for A_{sh}, it means the refrigerant is not heated enough to attain superheated state and the calculations should be done considering only the boiler and preheater segments. Where diverging, negative or complex values are obtained for A_b subsequently (using the same iterative approach as above), it can be concluded that the refrigerant is only heated in its liquid sate. Therefore the resultant output conditions of both refrigerant and water can be obtained by simply considering only the preheat segment where $A = A_{ph}$.

The accuracy of results from the steady state model could be confirmed by comparing with the test case depicted in Figure 15. Using the same inlet conditions presented in Section 3.1.4, Figure 17 compares steady state results obtained from the transient model (at different
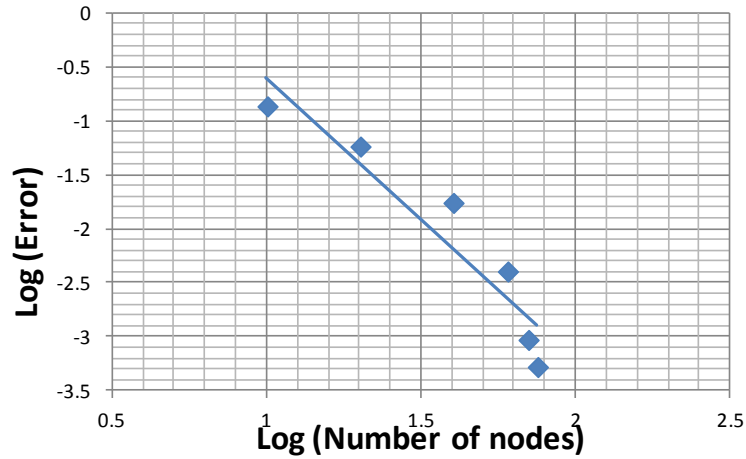
Figure 17: Comparison of steady state result with and transient model.

values of *N*) with the developed steady state model. It is seen that the developed steady state model can be as accurate as the transient model under constant input scenarios. In this case, the steady state model's estimation of $\dot{Q}_{in}$ is approximately same with that obtained with the transient model for *N* between 70-75.

3.2. The Condenser

As previously mentioned, the model represented by Figure 5 could also be adopted for a condenser in the developed ORC model with some slight changes. The case in the condenser presents a scenario where the heat transfer is from the refrigerant to water (cooling water in this case), again through the pipes. For the condenser, provision for the usual (encompassing) case is made; where phase change (condensation) of the refrigerant as it transits from a gaseous state to a liquid one.

3.2.1. NUMERICAL MODEL

Considering the same flow scenario of Section 3.1 for the evaporator, the solutions for the mass and energy equations of the mathematical models of Equations (21) - (26) remain valid also for the condenser, however due to the change in the direction of heat transfer, heat transfer terms of refrigerant-pipe and pipe-water could differ from those presented in Equations (24) and (26) as they witness a sign change. The heat transfer terms to be used for the condenser are given in Equations (64) and (65).

$$q_{w,i}{}^t = AH_w{}^t \left(T_{p,i}{}^t - T_{\mathrm{w},i}{}^t \right) \tag{64}$$

34

$$q_{ref,i}{}^t = AH_{ref,i}{}^t \left(T_{ref,i}{}^t - T_{p,i}{}^t \right) \tag{65}$$

Solutions of the condenser model will be similar to that of the evaporator as the devised solution approach will be used for the simulation with the same needed input parameters. It also follows that the representative block of Figure 6 also applies to the condenser.

3.2.2. HEAT TRANSFER COEFFICIENTS

A. Single phase heat transfer coefficient

Similar to the case of the evaporator, the heat transfer coefficients for the liquid water, liquid and gaseous refrigerant (single phase fluids) can be calculated using the Gneilinski equation (Equation (42)).

B. Two-phase heat transfer coefficient

As mentioned earlier, condensation of the gaseous refrigerant would occur in the flow which would require a different heat transfer coefficient model. As mentioned by Kakaç [33], calculating the heat transfer coefficient for the film condensation inside the tubes of the condenser would prove elusive if the flow pattern were not identified. The condensation flow pattern (misty, wavy, slug or bubble) was proposed to be identified with dimensionless mass velocity and Martinelli factor.

For simplicity this study would only distinguish the value of the condensation heat transfer coefficient based on Re_v. The Chato correlation is used for $Re_v < 35000$ given in [27] (p568) as;

$$H_c = 0.555 \left[\frac{g\,\rho_l\,(\rho_l - \rho_v)k_l{}^3 h_{lv}'}{\mu_l(T_{sat} - T_p)d_h} \right]^{0.25} \tag{66}$$

where T_{sat} is the saturation temperature at the given refrigerant hydraulic pressure and Re_v is defined by;

$$Re_v = \frac{\dot{m}\,d_h(x)}{A_{c,ref}\mu_v} \tag{67}$$

Also, the modified latent heat h_{lv}' is a function of latent heat h_{lv} given as;

$$h_{lv}' \equiv h_{lv} + {}^3\!/\!_8\,Cp_l\big(T_{sat} - T_p\big) \tag{68}$$

In [33], the constant (0.555) in Equation (66) was substituted by a parameter Ω for better accuracy given by;

$$\Omega = 0.728 \left[\frac{1}{1 + [(1-x)/x](\rho_v/\rho_l)^{2/3}} \right]^{3/4} \tag{69}$$

For higher Re_v (>35000), the Boyko & Kruzhilin correlation is used as presented in [2] given by;

$$H_c = \left(\frac{k_l}{d_h} \right) 0.021 Re_l{}^{0.8} Pr_l{}^{0.43} \left[1 + x \left(\frac{\rho_l}{\rho_v} - 1 \right) \right]^{0.5} \tag{70}$$
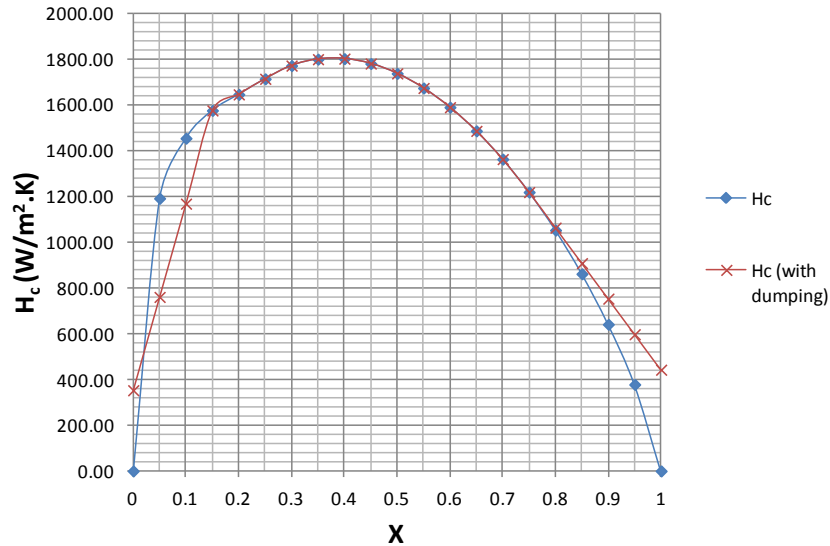

Figure 18: Variation of condensation heat transfer coefficient with vapour quality.

Similar to the case of the evaporator, a jump in the value of heat transfer coefficient can also be predicted for condensation, therefore dumping coefficients were also applied for regions of vapour quality below 0.15 and above 0.75. Figure 18 helps visualize the variation of condensation heat transfer coefficient with vapour quality in the modelled condenser for a test case; if R245fa condenses at 200kPa where d_i = 8 mm and $\dot{m}_{ref}$ = 0.01 kg/s at a constant pipe temperature of 15 ^{0}C.

3.2.3. SIMULATION RESULTS

The approximated (theoretical) condenser dimensions to be used for the condenser of the modelled ORC are presented in Table 9. Using these dimensions, a test simulation was also run to investigate the dynamics of the heat transfer towards steady state in a scenario,

where superheated refrigerant at 150 kPa and 40 ^{0}C enters to condense given inlet cold water of 15 kg/s at 20 ^{0}C and atmospheric pressure. The mass flow rate of refrigerant entering is once again 1.5 kg/s and was kept constant from one node to the other.
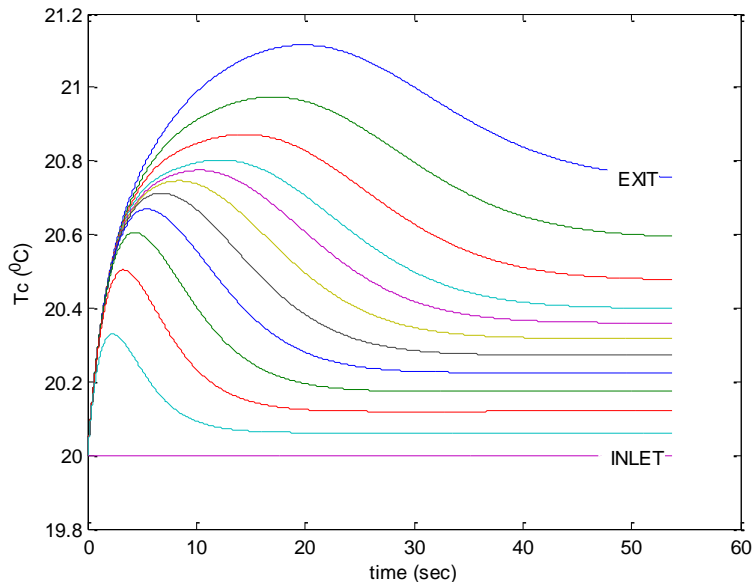

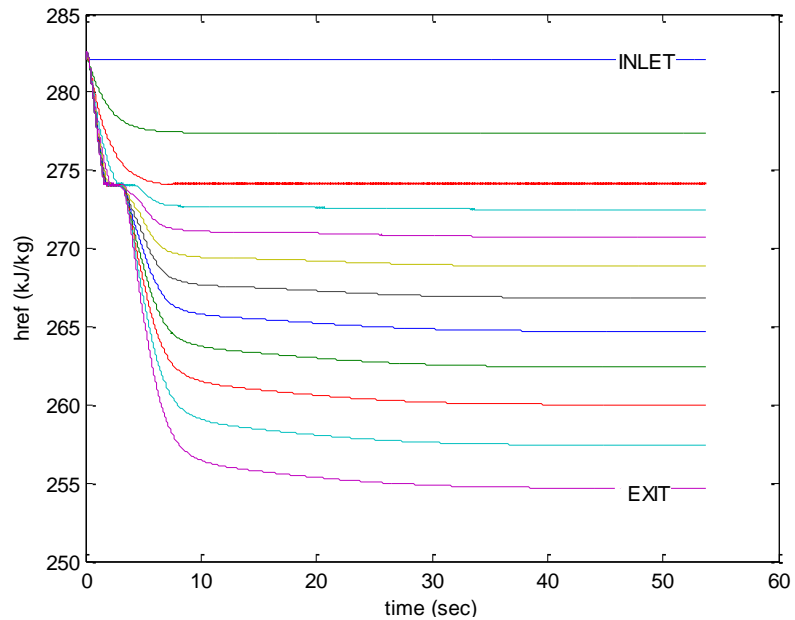Figure 19: Variation of cold water temperature.
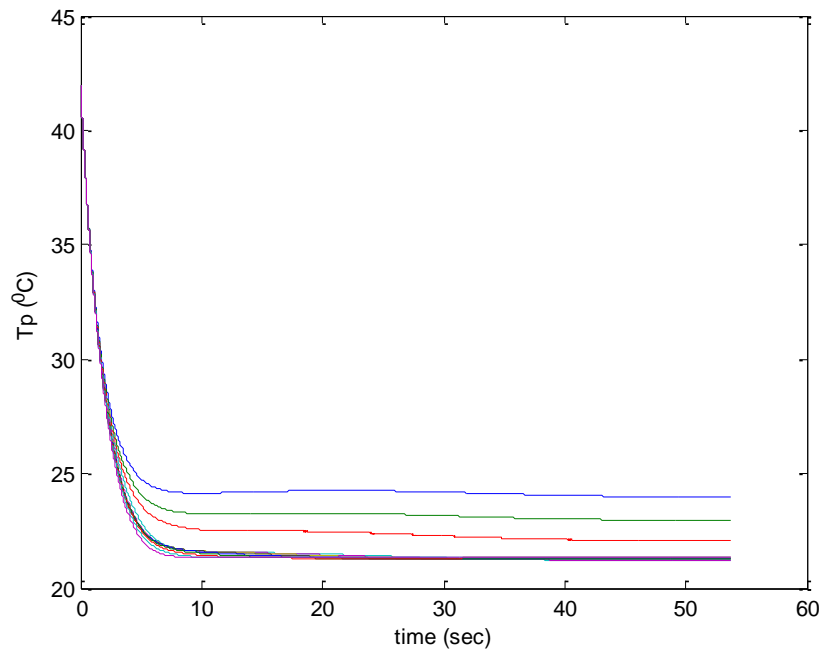

Figure 20: Variation of refrigerant enthalpy.

Figure 21: Variation of pipe temperature.

Figure 19 shows how the temperature of the cold water in each node varies and the simulation was truncated when the highest nodal difference experienced from one time step to the next becomes less than 0.0001^0C. This steadiness is seen to occur after 53.675 sec. Figure 20 shows the refrigerant exits as saturated mixture of 89.81 % quality at about 25.0879 ^{0}C (254.6557 kJ/kg). The pipe temperature varies as depicted by Figure 21.

Table 9: Condenser (theoretical) dimensions.

Parameter	Value	Parameter	Value
L	50.0000m	d	0.1235m
d_o	0.0686m	d_i	0.0656m

*Pipe material is stainless steel, A $\approx$ 11m^2.

3.3. The Pump

It is of popular knowledge that the pump performance/characteristic curves can be suitably used to model the operation of the pump as it was also mentioned in [30] that both turbo-machines in the cycle (pump and expander) can be adequately modelled as non-state

38

determinant. The pump characteristic curves referred to are the; *head-flow* and *efficiency-flow* curves, which are used to model the pump in this study.

3.3.1. NUMERICAL MODEL

Consider a sample head-flow rate curve for a pump operating at constant speed shown in Figure 22, a polynomial equation of this curve could be fitted to show the relationship of pump head (ΔH) with volume flow rate ($\dot{V}$).
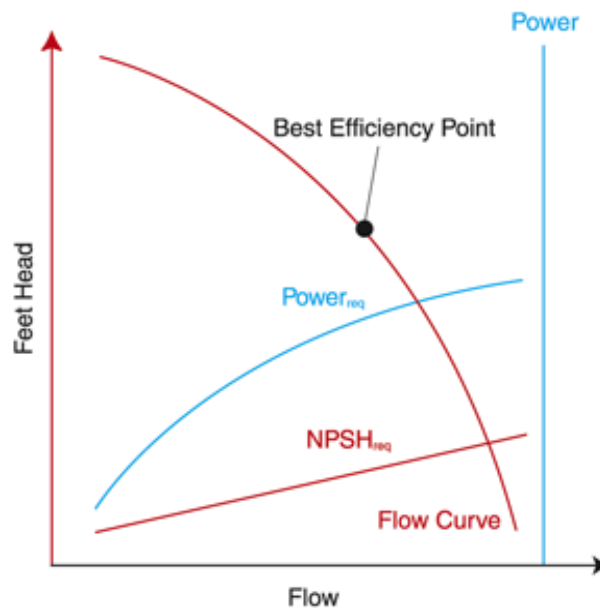

Figure 22: Typical pump performance plot.

Image from: *http://www.coleparmer.com/techinfo/techinfo.asp?ID=629&htmlfile=ReadPumpCurve.htm*

In this work, the refrigerant at the inlet of the pump is assumed to always be in saturated liquid state. This is a reasonable assumption, since the pump is to operate with single phase liquid and also, the thermodynamic properties of the refrigerant in the sub cooled state are obtained from their adjacent saturated liquid state values in this work. For a fitted polynomial of the form;

$$\Delta H \ = \ C_1 \dot{V}^2 + C_2 \dot{V} \ + \ C_3 \tag{71}$$

If the temperature of the inlet refrigerant is known, this equation could be manipulated to relate the pressure rise the refrigerant experiences from the pump and its mass flow rate given by;

39

$$\Delta P = (P_{pu,out} - P_{pu,out}) = g\left[\left(\frac{C_1}{\rho_{pu,in}}\right)\dot{m}^2 + C_2\dot{m} + C_3\,\rho_{pu,in}\right] \qquad (72)$$

Since $\rho_{pu,in}$ is a function of $T_{pu,in}$.

Since the 'black box' approach is suitable to model the pump as earlier mentioned, the actual exit conditions of the refrigerant from the pump and its ratio to the ideal (expected) conditions can only be determined after estimating the pump efficiency. This work combines the above devised ΔP-$\dot{m}$ equation with a mathematical model of the pump efficiency given by Quoilin et al. in [18].

If the pump hydraulic efficiency can be obtained experimentally from;

$$\eta_{pu} = \frac{\Delta P}{\rho_{pu,in}(h_{pu,out} - h_{pu,in})} \qquad (73)$$
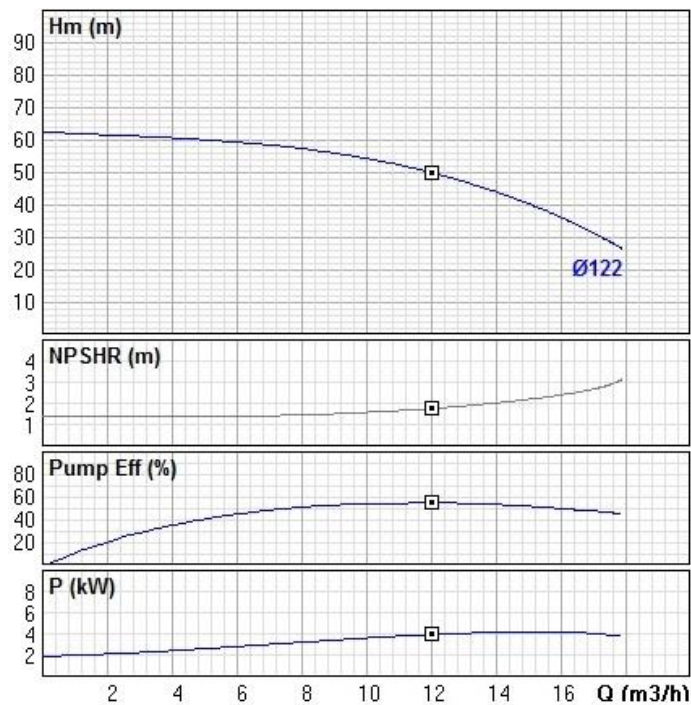
Figure 23: Characteristic curve of the selected pump.

A curve fit to model the efficiency as a function of a dimensionless parameter (Xpu) was proposed in Quoilin et al. in [18] to be of the form;

40

$$\eta_{pu} = A_0 + A_1.\log(Xpu) + A_2.\log(Xpu)^2 + A_3.\log(Xpu)^3 \qquad (74)$$

where Xpp was limited to be between 0.1-1 and given by;

$$Xpu = \frac{\dot{m}}{\rho_{pu,in}\dot{V}_{pu,max}} \qquad (75)$$

In order to calculate the actual electrical work required by the pump, the hydraulic efficiency, η, is multiplied by electromechanical efficiency to give an overall efficiency value.

The pump of the ORC unit that inspired this study is a multistage in-line pump with the following specifications; $\dot{V}_{pu,max}$ = 12m³/h, Power = 7.5kW. For this study, a pump with similar characteristics was selected using the *Standart Pompa Secim SPS* software. The pump characteristics curves also obtained from the software (shown in Figure 23) were used to obtain the constants in Equations (71) and (74) by regression.

From the selected pump's characteristic curves, the regression coefficients tabulated in Table 10 were obtained.

Table 10: Regression coefficients for the pump.

i	0	1	2	3
A	0.5430	-0.0722	-1.566	-1.2524
C	-	-796886	197.490	40.2660

The following block representation (Figure 24) for the pump model shows the inputs and obtained outputs.

INPUTS

$T_{pu,in}$, $P_{pu,in}$

Required $\dot{m}$

$h_{pu,in}$, $\rho_{pu,in}$

PUMP MODEL

OUTPUTS

$W_{actual,pu}$

$h_{pu,out}$

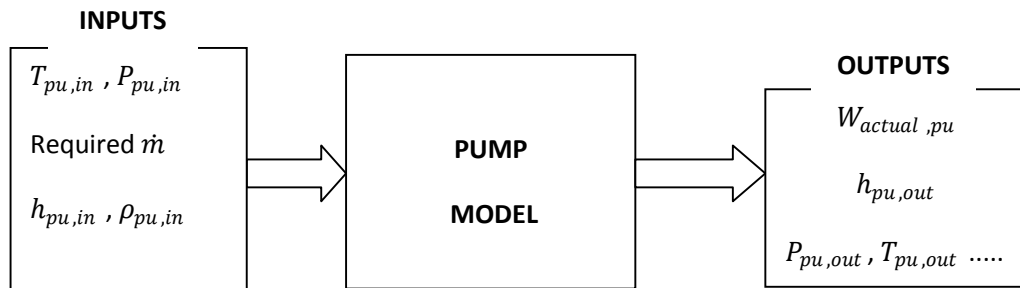$P_{pu,out}$, $T_{pu,out}$ .....

Figure 24: Block diagram of pump model.

3.4. The Expander

The expander of the inspiring ORC unit is a twin screw expander similar to that shown in Figure 25, Again a black box approach will be adequate to model the expander as the case of the pump.

Figure 25: Cut-out view of a twin screw expander.
Image source: *http://www.langsonenergy.com/white-paper*

A general relationship which can be expressed for the isentropic work of any turbine/expander operating in a Rankine (conventional/organic) is given as;

$$W_{isen,exp} = h_{exp,in} - h_{exp,out} \approx h_{ev,out} - f(s_{ev,out}, P_{exp,out}) \qquad (76)$$

Furthermore, the actual work output by the turbine can be calculated by discounting with isentropic and electromechanical efficiency terms given by;

$$W_{actual,exp} = \varepsilon_{em}\, \eta_{exp}\, W_{isen,exp} \qquad (77)$$

3.4.1. NUMERICAL MODEL

The task to find a model of the isentropic efficiency similar to Equation (74) could be fulfilled as done by Quoilin et al. in [34] where a polynomial for a curve fit of this variable was presented based on experimental testing on a scroll expander by Lemort et al. [35]. Based on pressure ratio over the expander (r_p) and density of inlet fluid to the expander, the

following curve fit that could be used for efficiency was given. Where $n=4$ was seen as adequate and a_{ij} and a_{0n} are the regression constants.

$$\eta_{exp} = \sum_{i=0}^{n-i}\sum_{i=0}^{n-1} a_{ij} . \ln(r_p)^i . \rho_{exp,in}{}^j + a_{0n} . \ln(r_p)^n + \rho_{exp,in}{}^n \tag{78}$$

This work will follow the study by Ng et al. [36] in modelling the turbine work and its efficiency. The reason is that the study applies directly to this work as it was a thermodynamic analysis of the performance of a screw expander tested with dry saturated steam. Following considerations of *over* and *under-expansion*, the nominal polytropic work output of the expander was given as a function of its in-built volume ratio (r_v) and again r_p as;

$$W_{poly,exp} = \left(\frac{P_{exp,in}}{\rho_{exp,in}}\right)\left(k - \frac{r_v}{r_p}\right) \tag{79}$$

where

$$k = \frac{r_v{}^{1-n} - n}{1 - n} \tag{80}$$

The "*polytropic expansion index*", n, accounts for the isentropic efficiency. Considering irreversibility or over/under-expansion losses, n is to be replaced by another index n_α to calculate the actual expander work output. From their experimental results using actual work output, n_α (called "*pseudo-polytropic expansion index*") was fitted using;

$$n_\alpha = \left[\frac{a_1}{log\ r_v} + \frac{a_2}{log\ r_v{}^2} + \frac{a_3}{log\ r_v{}^3}\right] log\ r_p \tag{81}$$

For the purpose of this study, the regressed constants a_1 - a_3 that will be used are;

Table 11: Regression coefficients for expander index.

	1	2	3
a	8.74 E -2	1.45 E -1	2.41 E -1

As seen from all established considerations of this section, this work does not consider any variation in refrigerant mass flow rate through the expander due to the black box approach taken. The model block for the expander is shown in Figure 26.
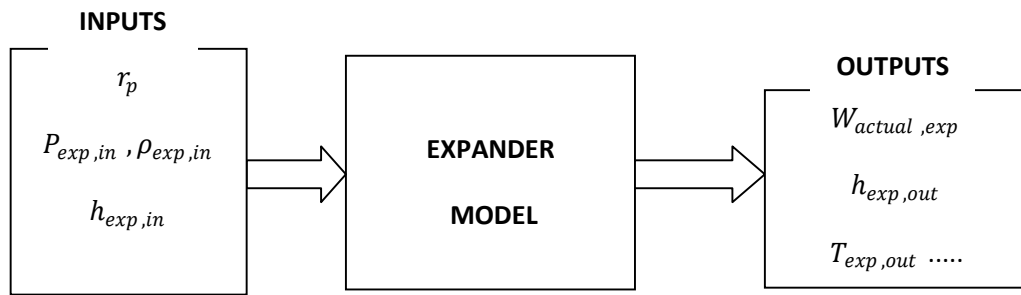
Figure 26: Expander block representation.

CHAPTER 4

4. INVESTIGATIONS USING THE ORC MODEL

The individual component models from Chapter 3 were written as functions with the required inputs and outputs at each stage as seen in Figure 27 (where *Y* in the figure represents other thermo-properties of the fluid not shown).
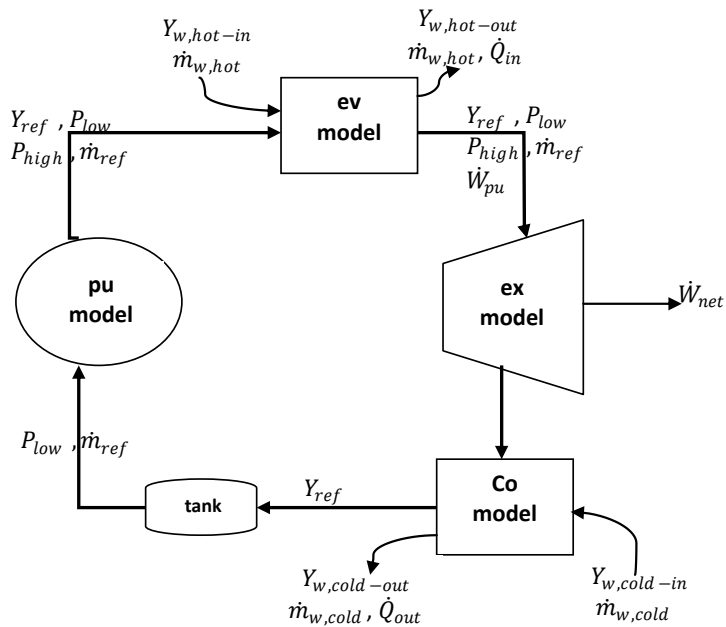

Figure 27: Schematic of ORC model showing state variables.

The functions were eventually brought together in another code to simulate the full ORC system as represented in Figure 28. In this chapter, the ORCs performance under different given operation scenarios will be investigated in two consequent stages. These are namely steady and transient operations of the ORC.

Steady operation scenario is possible in the solar ORC under study when a supplementary boiler is considered to help keep the heat input conditions stable while a dynamic investigation is necessary otherwise. The investigations based on steady input scenarios will

help visualize an overview of the system's performance in the considered operating temperature range and identify influences of critical parameters to the system's operation. On the other hand, the main goal of dynamic analyses is usually to investigate the transient responses of the system to changes in the identified critical parameters, and possible control strategies as seen in [18]. By combining the representative blocks from all components, the possible inputs and outputs to the ORC model is seen in representative block of Figure 28.

INPUTS

$\dot{m}_{ref}, T_{low}$ or P_{low}

$T_w, P_w, \dot{m}_{w\,hot-in}$

$T_w, P_w, \dot{m}_{w\,cold-in}$

ORC MODEL

OUTPUTS

W_{net}

η_{cycle}

State variables.....
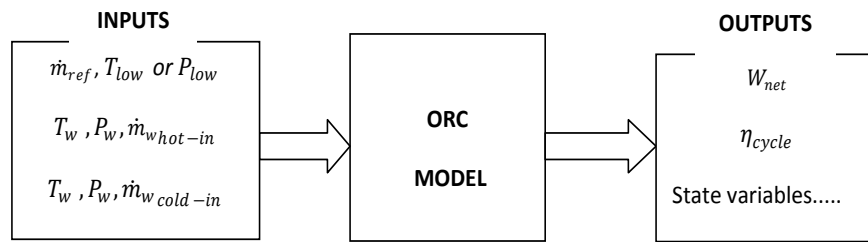
Figure 28: Block diagram of ORC model.

Considering the ambient temperature and the refrigerant properties, a condenser pressure, P_{low} (150 kPa) was imposed on the ORC model for all simulations. All investigations are performed considering the following physical constraints and nominal operating conditions.

a. Pump; $\dot{m}_{ref}$ possible between 0.5-1.5 kg/s.

b. Solar field; $\dot{m}_{w,hot}$ between 2-12 kg/s and $T_{w,hot-in}$ between 80-95 ^{0}C at 100 kPa.

c. Cooling Tower; $\dot{m}_{w,cold}$ fixed at 15 kg/s, $T_{w,cold-in}$ at 20 ^{0}C and 100 kPa.

4.1. Steady State Analysis

Steady state analysis of the ORC unit is performed to define the feasible operation scenarios in the considered operating conditions. These conditions are a combination of the following critical parameters; mass flow rate of the water in the solar field circulation ($\dot{m}_{w,hot}$), mass flow rate of the refrigerant in the ORC unit ($\dot{m}_{ref}$), and the temperature of water at the inlet of the evaporator unit ($T_{w,hot-in}$).

The aim of this analysis is not only to identify a single set of values of these parameters that gives the best cycle performance, but also to visualize their influences which can further define changes that could be made to ensure a feasible steady state operation given any

level of available input. The parameters related to the solar field circulation; $\dot{m}_{w,hot}$ and $T_{w,hot-in}$, characterize the energy input to the ORC unit and hence are critical for investigating the size requirements of the solar field and the backup boiler. The mass flow rate of the refrigerant ($\dot{m}_{ref}$), determines the pressure levels of the evaporator and the condenser and hence is critical for the power production capability of the ORC unit. The combination describes the thermal efficiency of the cycle, as defined in (82).

$$\eta_{cycle} = \frac{\dot{W}_{net}}{\dot{Q}_{ORC,in}} = \frac{\dot{W}_{exp} - \dot{W}_{pu}}{\dot{Q}_{ORC,in}} \qquad (82)$$

4.1.1. INFLUENCE OF HOT WATER TEMPERATURE

In a number of ORC performance investigations studies like in [37], the evaporating temperature is usually selected a critical parameter. At steady state, it is determined by the variables of interest already selected in this study. Given a fixed low pressure of operation, it is expected that the power output improves with better heat input (indicated by higher $T_{w,hot-in}$). A plot of simulation results demonstrates conformity to this expectation. In Figure 29, it is observed that the evaporator effectiveness increases with $T_{w,hot-in}$, as a result higher heat input to the system is achieved with increasing $T_{w,hot-in}$ irrespective of combination of values of $\dot{m}_{ref}$ and $\dot{m}_{w,hot}$ that define dimensionless mass flow ratio M (as seen in Equation (83)).

$$M = \frac{\dot{m}_{ref}}{\dot{m}_{w,hot}} \qquad (83)$$

The resultant influence on the cycle efficiency can be seen as expected in Figure 30, which also indicates antagonistic effect of dimensionless mass flow ratio (*M*) approaching to zero and approaching to one or more on the entire cycle. Deductions from these reaffirmations suggest that maximum exploitation of the power production potential should be the goal for any level of available heat input, especially when it is high. Following numerical analysis on the results described in Figure 29, the evaporator effectiveness can be defined using regression by Equation (84) in the considered operating conditions. Where, $T_{w,hot-in}$ is expressed in (^{0}C) with R^2 = 0.9884.

$$\varepsilon = -3.18E^{-2} \, M^2 T_{w,hot-in} + 2.44 \, M^2 + 2.92E^{-2} \, M \, T_{w,hot-in} - \qquad (84)$$
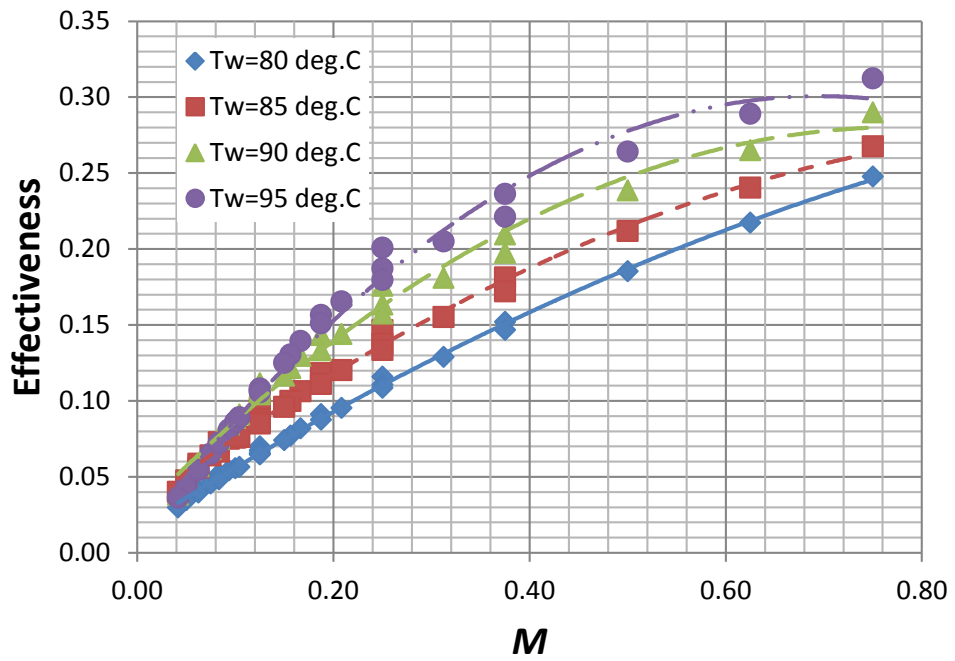$$1.96 \, M - 4.71E^{-4} T_{w,hot-in} + 6.26E^{-2}$$

Figure 29: Effectiveness of evaporator as a function of hot water inlet temperature and dimensionless mass flow ratio.
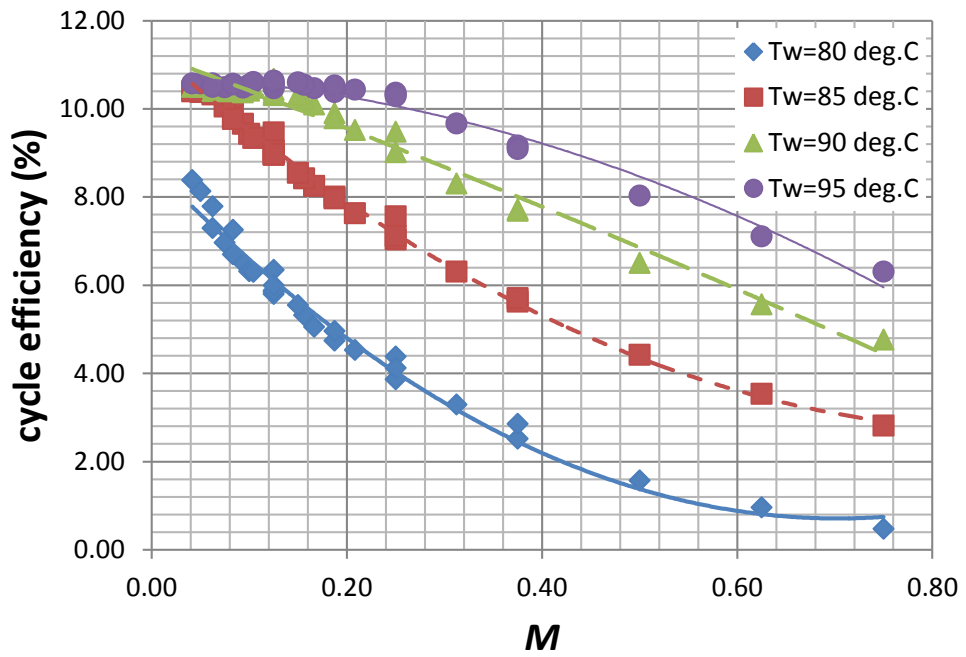

Figure 30: Cycle efficiency as a function of hot water inlet temperature and dimensionless mass flow ratio.

Figure 29 suggests higher evaporator effectiveness, ε, for higher mass flow ratios, showing the evaporator becomes less effective when the refrigerant mass flow rate ($\dot{m}_{ref}$) is much smaller than the mass flow rate of the hot water, $\dot{m}_{w,hot}$. (i.e. $T_{w,hot-in}$ drop is higher). Figure 30 on the other hand shows that the resulting cycle efficiency reduces with increasing the mass flow rate ratio, M. This is due to the fact that the refrigerant flow is too 'fast' to gather energy from the hot water in the evaporator.

4.1.2.   INFLUENCE OF HOT WATER FLOW RATE

Based on the defined upper and lower limits for inlet hot water temperature and refrigerant mass flow rate (Page 46), four cases are evaluated with varying hot water mass flow rate, $\dot{m}_{w,hot}$.

   a. $T_{w,hot} = 95\,^{0}\text{C}$ and $\dot{m}_{ref} = 0.5$ kg/s (**Case A**).
   b. $T_{w,hot} = 95\,^{0}\text{C}$ and $\dot{m}_{ref} = 1.5$ kg/s (**Case B**).
   c. $T_{w,hot} = 80\,^{0}\text{C}$ and $\dot{m}_{ref} = 0.5$ kg/s (**Case C**).
   d. $T_{w,hot} = 80\,^{0}\text{C}$ and $\dot{m}_{ref} = 1.5$ kg/s (**Case D**).

The results are presented in Figure 31 to Figure 34 for cases (A-D) respectively. For all cases, heat input to the ORC unit, $\dot{Q}_{ORC,in}$, increases with inlet hot water mass flow rate, $\dot{m}_{w,hot}$ since it defines the available heat resource in conjunction with $T_{w,hot-in}$. There is a higher 'potential' to produce more work with higher $\dot{m}_{w,hot}$. As P_{low} is fixed in all cases, the net power produced will be solely dependent on the thermodynamic state at the inlet of the expander (also corresponds to exit of the evaporator as depicted in Figure 1, in Page 2). Even as high refrigerant temperatures can be reached at the expander inlet, the actual heat transfer (from water to refrigerant) in the evaporator may become less effective (depending on the corresponding $\dot{m}_{ref}$ used). This would diminish η_{cycle} as seen in Figure 31 and Figure 32 where there is negative or zero marginal increase in the cycle efficiency after a certain $\dot{m}_{w,hot}$ value.

At low refrigerant mass flow rates (Figure 31 and Figure 33), the heat input to the cycle is reduced compared to the adjacent scenarios (Figure 32 and Figure 34) where refrigerant flow rate is high. An important use of the results for these cases help us identify that an optimum hot water mass flow rate exists to operate the system at steady state given a high/low level of available heat input, For instance, when heat source is only solar based or solar supplemented by boiler.
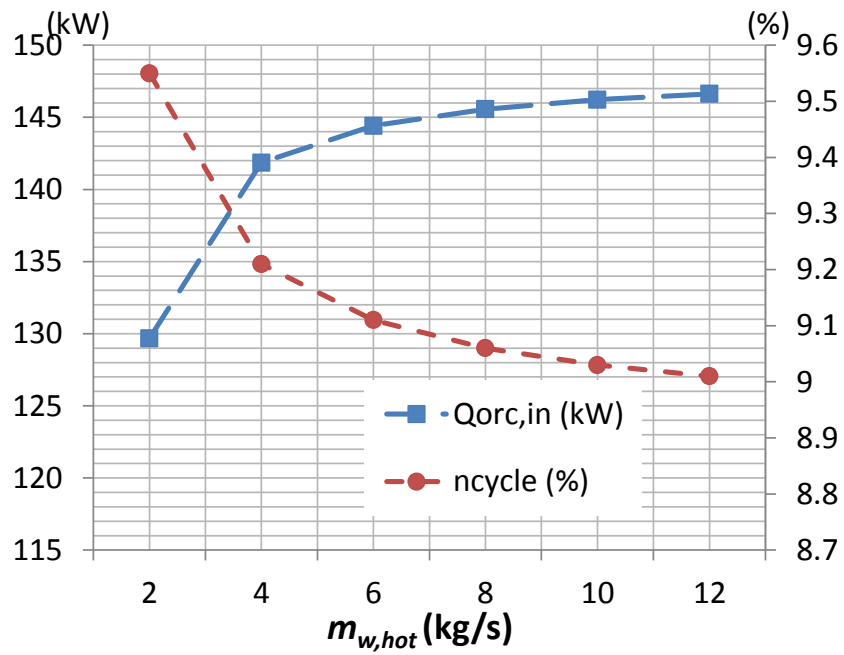
Figure 31: Influence of hot water flow rate for $T_{w,hot} = 95\ ^0C$ and $\dot{m}_{ref} = 0.5$ kg/s.
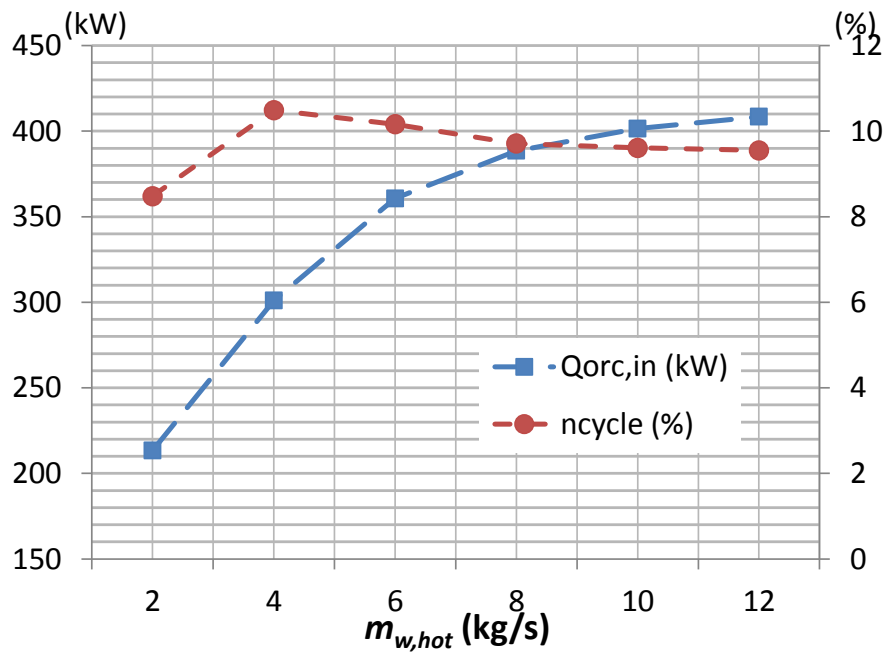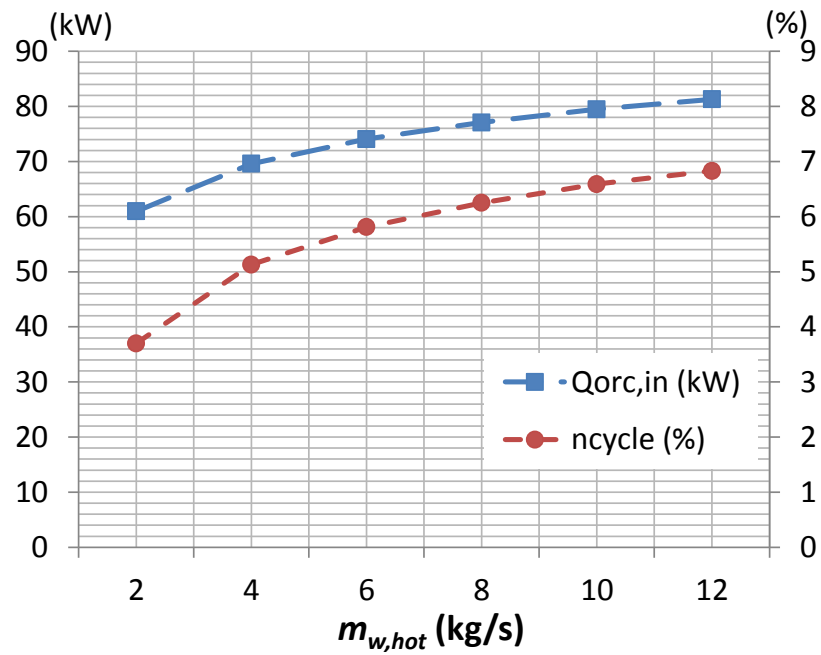

Figure 32: Influence of hot water flow rate for $T_{w,hot} = 95\ ^0C$ and $\dot{m}_{ref} = 1.5$ kg/s.

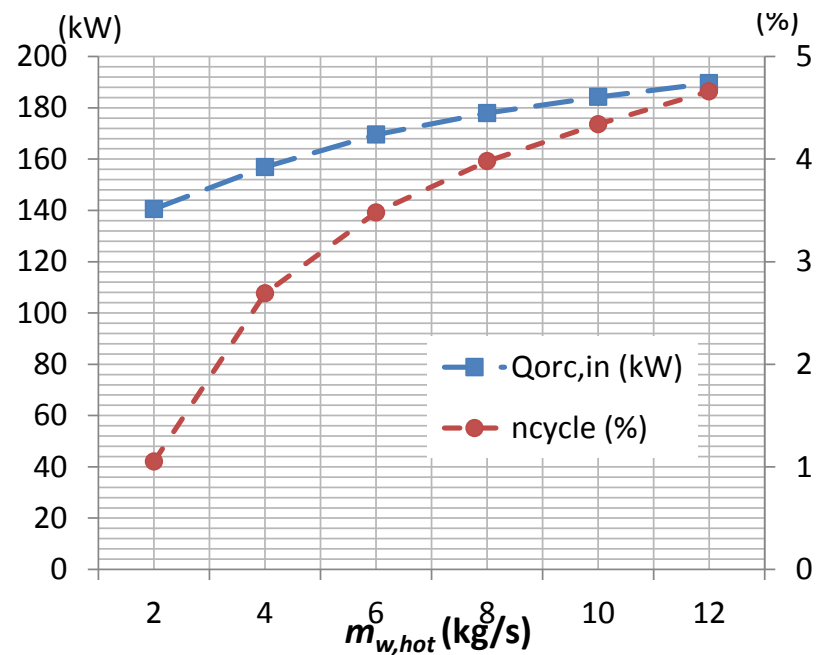Figure 33: Influence of hot water flow rate for $T_{w,hot} = 80\ ^0C$ and $\dot{m}_{ref} = 0.5$ kg/s.

Figure 34: Influence of hot water flow rate for $T_{w,hot} = 80\ ^0C$ and $\dot{m}_{ref} = 1.5$ kg/s.

4.1.3.   INFLUENCE OF REFRIGERANT MASS FLOW RATE

This investigation reemphasizes the antagonistic effects of mass flow ratio (*M*) on the cycle as it intends to extract the sole influence of refrigerant mass flow rate. Figure 35 to Figure 37 show area plots of accepted heat input and cycle efficiency for minimum, median and maximum possible $\dot{m}_{ref}$ values (0.5, 1 and 1.5 kg/s respectively). Results for other $\dot{m}_{ref}$ values (0.75 and 1.25 $\mathrm{kg/s}$) can be found in Appendix. Higher heat input is recorded as $\dot{m}_{ref}$ changes from its minimum to its allowable maximum as hinted in the previous investigation of section 4.1.2. However, the cycle efficiency does not follow this trend with increasing refrigerant mass flow rate. This is due to the increase of *M* for a fixed value of hot water flow rate as refrigerant flow rate is increased. It is confirmed that the increase in heat input counterbalances the decrease in cycle efficiency because the resulting net work output has been observed to increase. This is known by overlapping the area plots of $\dot{Q}_{ORC,in}$ and η_{cycle}, based on the definition of η_{cycle} in Equation (82).

4.2. Transient Analysis

Transient analysis is performed using the transient heat exchanger models with steady models shown for the pump and expander. This is valid due to the fact that the response time of the turbo-machinery is assumed to be very small compared to the heat exchangers. In this section, the system transient response to different test scenarios defined by unsteady heat input would be evaluated.

4.2.1.   SAMPLE DYNAMIC SCENARIO (RAMP-UP & RAMP-DOWN)

The investigation attempts to simulate the response of the system in scenarios similar to occurrences during system start-up and system shut-down. Where both cases are characterized by linear increase (ramp-up) and decrease (ramp-down) of hot water inlet temperature with time respectively. For the system running at flow rates, $\dot{m}_w$ = 12 kg/s and $\dot{m}_{ref}$ = 1.5 kg/s, the scenario considers the linear increase/decrease of $T_{w,hot-in}$ between 80 ^{0}C to 95 ^{0}C.

The initial condition for the evaporator model considers constant temperature profile based on the inlet conditions of the refrigerant and the hot water inflows into the counter-flow heat exchanger. Figure 38 and Figure 39 show the transient response of the ORC unit for both cases (ramp-up and ramp-down) respectively, which can be visualized accurately only after allowing the system to achieve steady state at stable inlet conditions before varying those conditions. To minimize the influence of the initial condition effects, the solution for each case runs the system at the first heat input for twice the time frame it achieves steady state
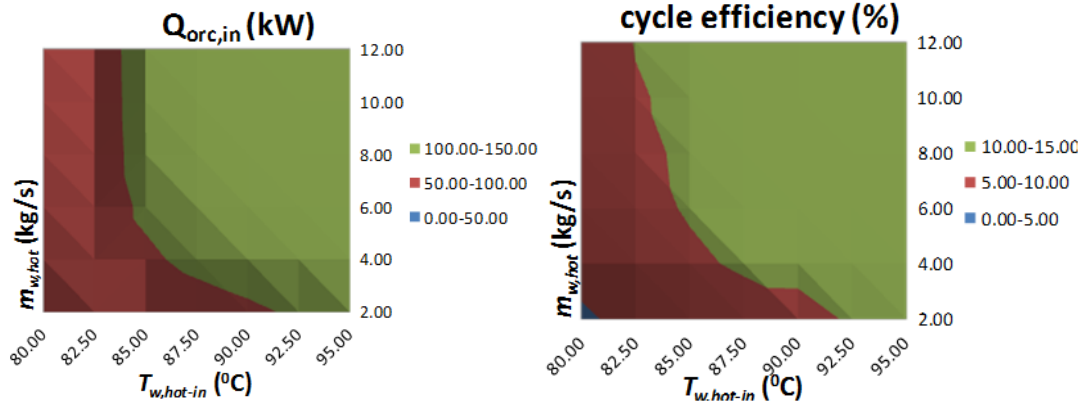
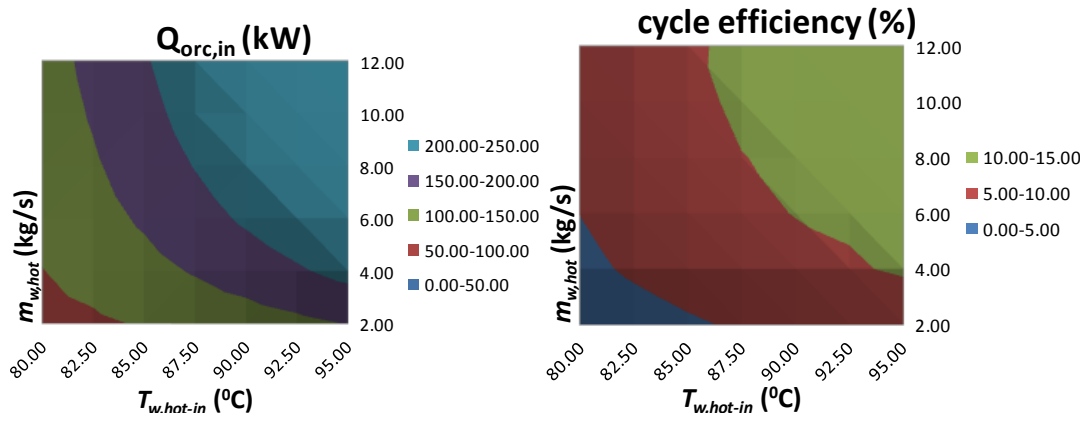**Figure 35:** Heat input and cycle efficiency for minimum refrigerant flow rate (0.5 kg/s).

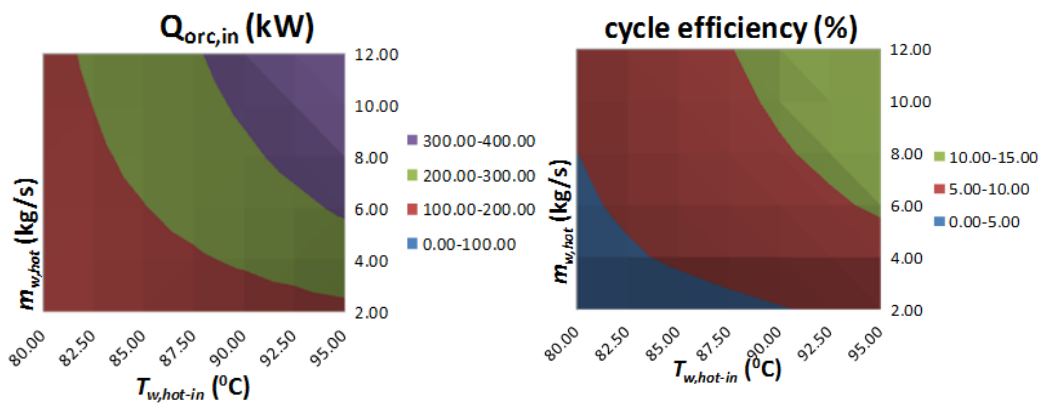**Figure 36:** Heat input and cycle efficiency for median refrigerant flow rate (1 kg/s).

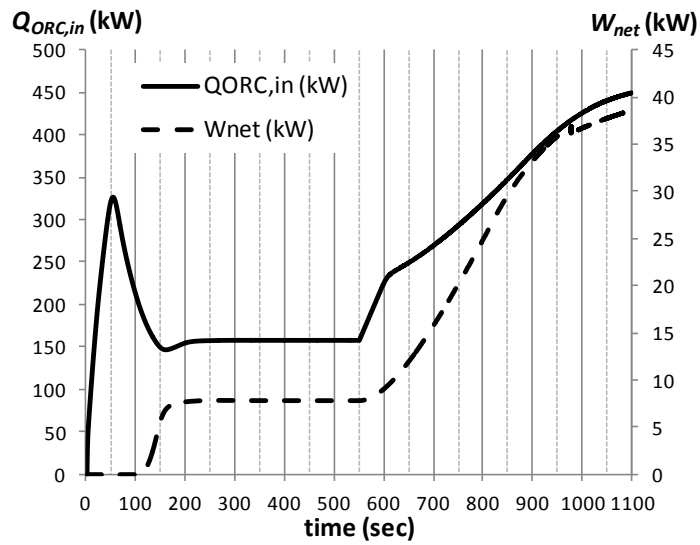**Figure 37:** Heat input and cycle efficiency for maximum refrigerant flow rate (1.5 kg/s).

Figure 38: Transient response during ramp-up.

$(2t_{ss})$ before enforcing either ramp-up/down for a further $2t_{ss}$. This corresponds to about 550 sec for ramp-up as seen in Figure 38 and 400 sec for ramp-down as in Figure 39.
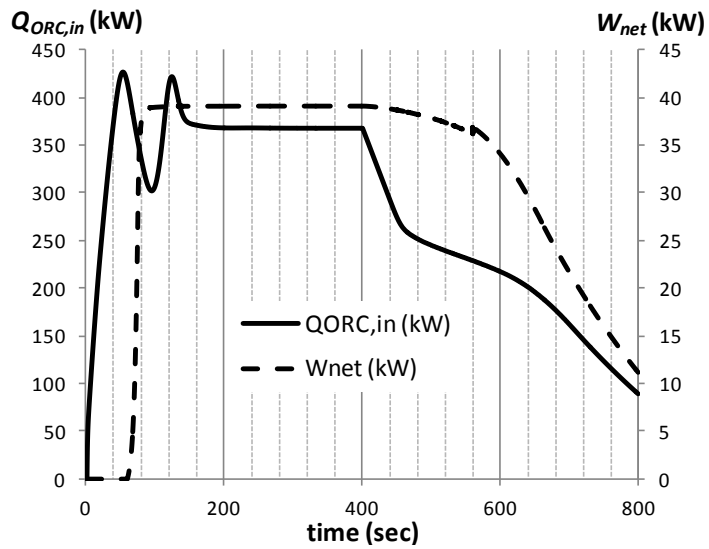

Figure 39: Transient response during ramp-down.

For both cases, it is expected that cycle output follows the increasing or decreasing trend enforced by the ramp-up or ramp-down. However, it can be deduced from both Figure 38

and Figure 39 that there is a lag in the response of instantaneous cycle efficiency (instantaneous ratio of $\dot{W}_{net}$ to $\dot{Q}_{ORC,in}$) before it concurs to the trend. This shows the combined influence of a change in the evaporator effectiveness with change in absolute value of heat input, $\dot{Q}_{ORC,in}$, after the thermal capacitance (prior to ramp-up/down) has been expended. The lag is also observed to be for a shorter duration during ramp-up compared to during ramp-down.

4.2.2.   DYNAMIC SCENARIO WITH CONTROL MEASURE

Furthermore, another transient scenario is carried out to make use of previously obtained steady state analysis results. In this scenario, available heat source drops from a high value to a lower one (from about 360kW to 200kW), similar to the occurrence when the ORC operating solely on solar energy resource has its PTC collectors briefly shaded by clouds. Running at hot water flow rate, $\dot{m}_w$ = 10 kg/s and refrigerant flow rate, $\dot{m}_{ref}$ = 1.5 kg/s, Figure 40 shows the ensuing temperature change defining the occurrence. For this drop in the heat input, previous steady state discussions proposes reducing M to help extract more work given the new (lower) heat input value.
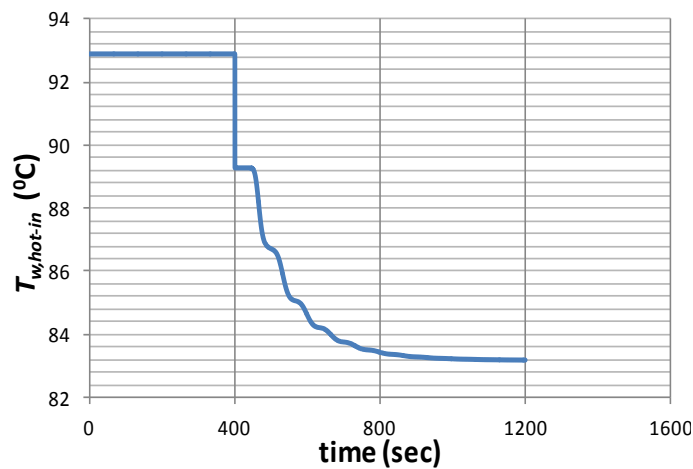

Figure 40: Inlet hot water temperature profile when available heat source experiences a sudden drop.

As seen in Figure 41, the solution approach enforces the sudden drop in heat input ($\dot{Q}_{ORC,in}$) after the system has fully responded to the initial condition (for 400 sec.) where cycle net power output ($\dot{W}_{net}$) is about 38.5kW. The system is then allowed to run for a further 800secs without any change in mass flow rates (for comparison) to show a steady $\dot{W}_{net}$ of 14.7kW. At 1300secs the control measure is enforced; $\dot{m}_w$ is increased to 12 kg/s and $\dot{m}_{ref}$

reduced to 1.39 kg/s (decreasing M). Operation after a further 700sec indicates a full system response to produce about 15.6kW (corresponding to η_{cycle} of 7.9%). This confirms the potency of the control measure as identified from steady state analyses.
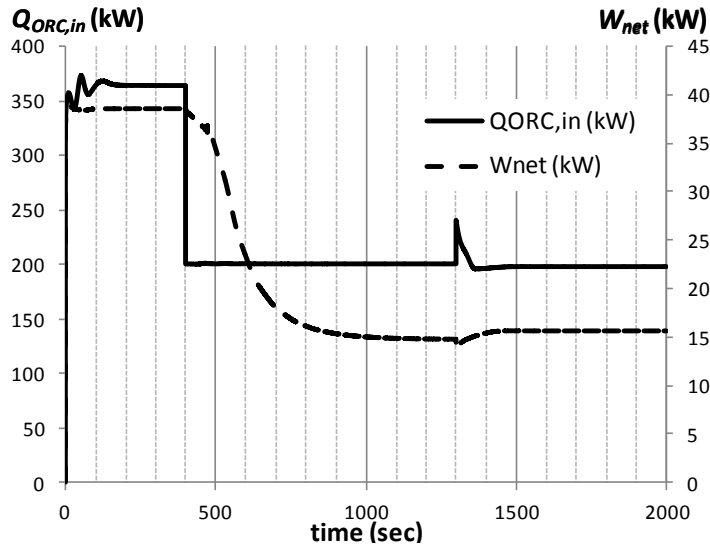

Figure 41: Transient system response for dynamic scenario with control measure.

4.2.3. ADVANTAGE OF CONTROL MEASURE

Following confirmation of the potency of control measures in section 4.2.2, in the event of a real-time variable heat input occurrence, the potential benefit of enforcing control measure can be further demonstrated with simulation of another dynamic scenario. It should be noted that the investigation in section 4.2.2 is based on the assumption that the heat supplied (irrespective of source combination) is capable of rendering the instantaneous required heat input $\dot{Q}_{ORC,in}$ of the system.

Although the present thesis has drawn its boundary of analysis to consider only the ORC unit in the entire solar-thermal system, results would be better related to if a simplified relationship was established between available heat input (in the hot water loop) $\dot{Q}_{av}$ and that transferred to the refrigerant loop $\dot{Q}_{ORC,in}$. The two distinct variables can be understood from Figure 42 while equation (85) presents how the inlet hot water temperature to the ORC $T_{w,hot-in}$ could vary with $\dot{Q}_{av}$ and the selected flow rate, $\dot{m}_{w,hot}$ .Using the previous assumption stated for section 4.2.2, it follows that;

$$T_{w,hot-in}{}^{t+1} = \frac{\dot{Q}_{av}{}^{t+1}}{\dot{m}_{w,hot}Cp_{w,hot}{}^{t}} + T_{w,hot-out}{}^{t} \tag{85}$$
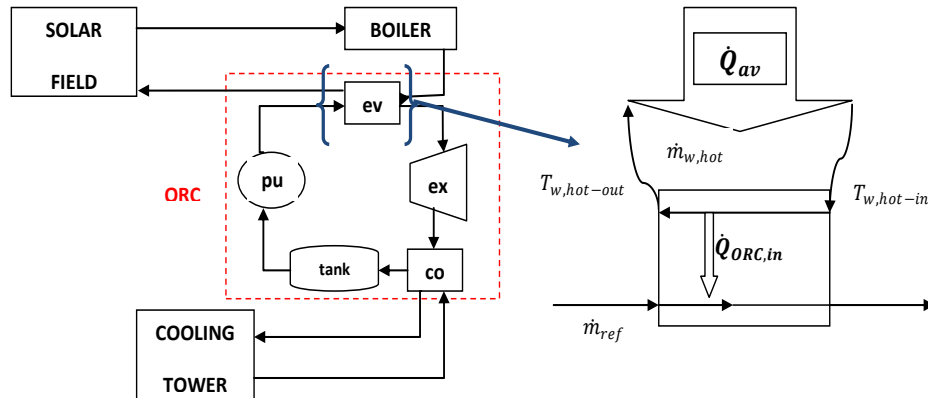

Figure 42: Representation of hot-water loop.

Subsequently to establish comparison, a case with no control measure (NCM); where only $T_{w,hot-in}$ changes with fixed flow rates, will be compared to a case where flow rates (hence flow ratio) are controlled (CM) simultaneously as $T_{w,hot-in}$ changes. The variable available heat ($\dot{Q}_{av}$) profile to be used is shown in Figure 43, while Figure 44 and Figure 45 show inlet hot water temperature and flow rate transitions respectively for the scenario with control measure (CM) and that with no control measure (NCM).
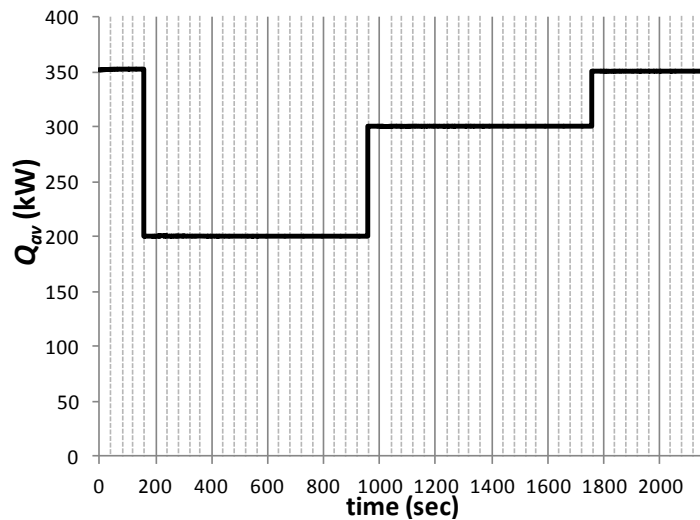

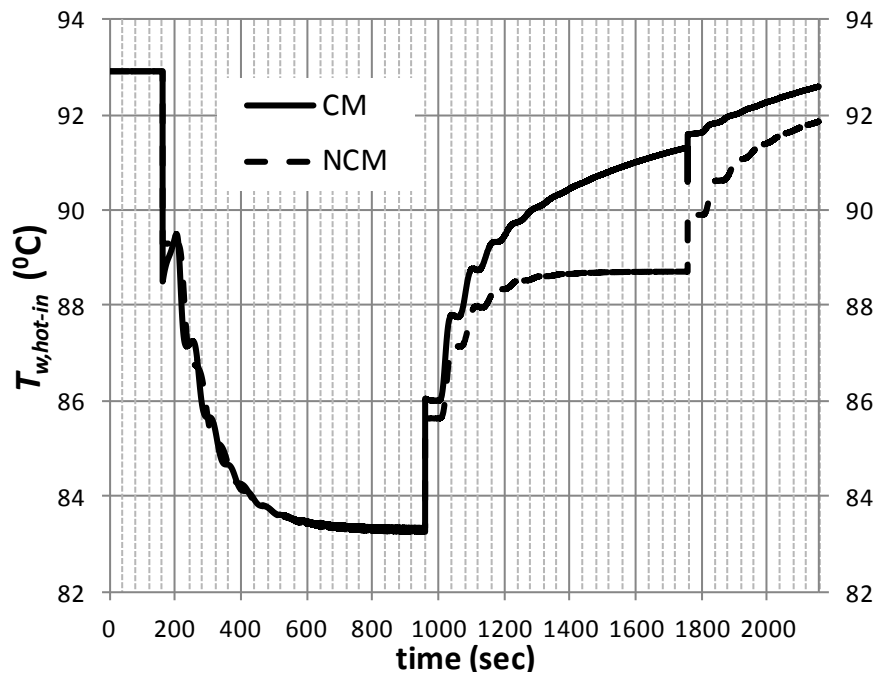Figure 43: Available heat input profile.

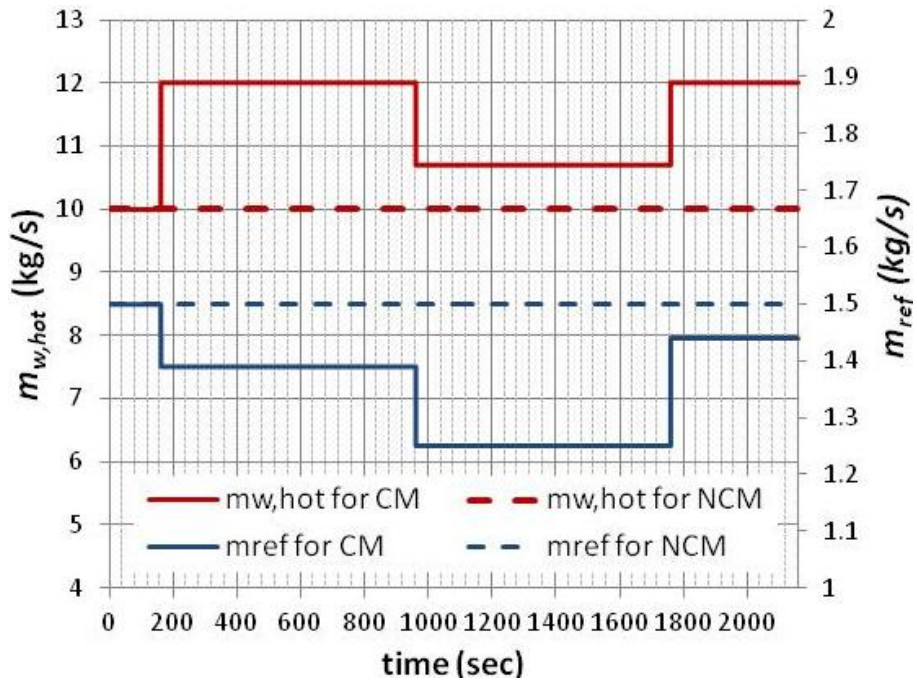Figure 44: Hot water inlet temperature transition for CM and NCM.

Figure 45: Mass flow rate profile for CM and NCM.

As seen in Figure 45, the NCM simulation was run at $\dot{m}_{w,hot}$ = 10 kg/s and $\dot{m}_{ref}$ = 1.5 kg/s. For the CM case, $\dot{m}_{w,hot}$ and $\dot{m}_{ref}$ were changed to 12 kg/s and 1.39 kg/s respectively when $\dot{Q}_{av}$ dropped to 200 kW (at 160 sec). When $\dot{Q}_{av}$ became to 300 kW, $\dot{m}_{w,hot}$ = 10.7 kg/s and $\dot{m}_{ref}$ = 1.25 kg/s and 2000 sec when $\dot{Q}_{av}$ recovered to 350 kW, $\dot{m}_{w,hot}$ and $\dot{m}_{ref}$ were changed to 12 kg/s and 1.44 kg/s respectively.

As seen in Figure 46, net power production under CM scenario appears to outperform net power under NCM scenario, especially at instances before full system response to the sudden change in available heat input. Furthermore, Figure 47 depicts the difference in power output obtained from applying CM as compared to NCM which confirms the potential benefit/superiority of enforcing control measures when available heat input is variable. Numerical approximation of the area under the graphs in Figure 43 and Figure 46 yields an approximate value of 597 MJ for the total energy available (E_{av}), while net recovery under CM (E_{CM}) and NCM (E_{NCM}), are 59 MJ and 58 MJ respectively. It is worthy of note that the aforementioned potential benefit could be reduced if the power requirement to provide the change in $\dot{m}_{w,hot}$ (from the hot water loop pump) is considered.
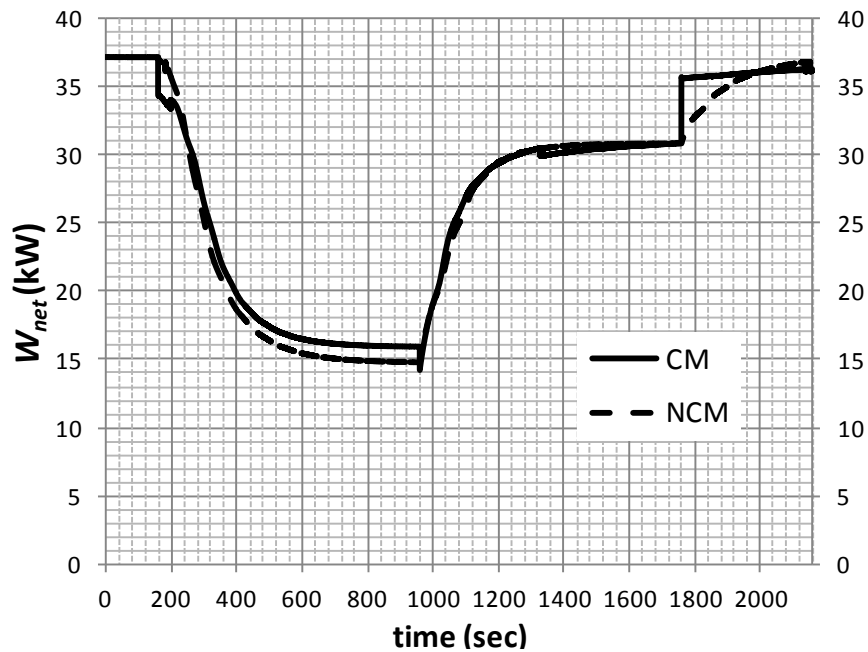

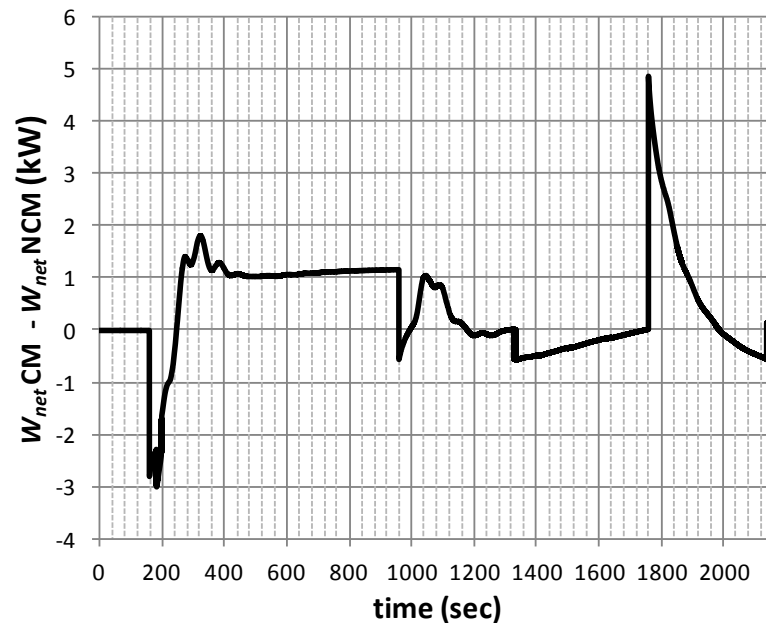Figure 46: Net power output under CM and NCM.

Figure 47: Difference in power output from CM to NCM.

CHAPTER 5

5. CONCLUSION AND RECOMMENDATION

This study has synthesized a solar organic Rankine cycle (ORC) model via sub-models of its main components (pump, evaporator, expander and condenser) with bases in the thermo-physical property calculations of its working fluid (R245fa) which have also been presented. The present study intends to serve as a manual on numerical modelling of solar ORC units as it presents modelling approaches applicable for both steady and transient operation of the cycle. Both modes of operation have been taken into account given that heat input to the ORCs could be stable or vary in time depending on the choice/combination of heat source used.

Since the energy interactions in the generic ORC are deduced from the properties of its working fluid defining different states in the cycle, it was essential that a module to calculate these properties be readily available to the ORC model. This study applied regression based models for the calculations, which provides economical use of computational resources since properties can be defined for specific range of interests. Properties on the saturation dome of the fluid were defined with quadratic functions of either saturation temperature or pressure, while critical properties of the fluid in the superheated region were estimated using two variable non-linear functions. It was discovered that these two-variable functions could also be applied for the compressed liquid state as they can also be approximated by their adjacent values on the saturation dome.

Due to the fact that the transient response time of the pump and expander are shorter that the heat exchangers (evaporator and condenser) of the ORC, it is seen that the heat exchanger models are the critical components in investigating the steady or transient mode of operation since they are the principal media of heat transfer in and out of the ORC. The resultant steady state versions of their models have been established based on an iterative ε-NTU method and the transient versions are finite volume based (all considering phase change of the refrigerant). Observations have shown that both models (steady and transient) are consistent in predicting the heat transfer involved through the 'consistency tests' performed. Thermodynamic models of the selected pump and expander have also been highlighted with strong bases in literature and they all have proved adequate to model the system under the given nominal operating conditions/enforced constraints.

61

Investigations performed following integration of the ORC model have used the steady state models to present an overview of the cycle performance by devising a map of feasible operation ranges which can be used for general decision making process. These operation ranges are defined in terms of the identified critical parameters (inlet hot water temperature, mass flow rates of both refrigerant and water). The present study has also investigated the effect of these critical parameters on the cycle performance. It is concluded from the analyses that; the results can be used to define control measures which can ensure an optimum power output range or steady operation given any level of heat input, either stable or variable.

Since the ORC unit of the present study is considered primarily for power production, results indicate a maximum steady state efficiency of 10.5 % compared to its Carnot efficiency of about 20 % (based on highest temperature difference). Its peak power production is about 40 kW as seen under specified operation scenarios. It should be noted that, the present study does not include the influence of other minor power consuming equipments in the solar thermal system. Also economical constraints which dictate a minimum value of power produced are not considered. Further research as a follow-up to this study could consider these constraints.

The most apparent future research venture would be experimental validation of the developed ORC model and its modelling approaches. Recommendation for other future follow-up studies are;

    a. Broadening the investigation horizon to include the solar collector and cooling tower loop.
    b. Consequent location-wise performance study and optimization.
    c. Further study on the expander performance.
    d. A more focused view at phase change heat transfer.
    e. Correlation of the model to the real system measurements.

REFERENCES

1. **U.S. Energy Information Administration.** *Annual Energy Review 2009.* 2010. pp. Tables 1.3, 2.1b-2.1f, 10.3, and 10.4.

2. *Solar Energy Utilization in Agriculture in Nigeria.* **F., Sheyin.** Brighton : Elsevier Science Ltd., 2000. World REnewable Energyg conference VI (WREC2000).

3. **David J. Bennett, David A. Eijadi.** *Passive solar lighting system. 4329021* U.S.A, 11 May 1982.

4. *Photovoltaic systems for distributed power supply in Nigeria.* **O, Oparaku.** s.l. : Eselvier, 2002, Renewable Energy, Vol. 25, pp. 31-40.

5. **Hsieh, J. S.** *Solar Energy Engineering.* s.l. : Prentice Hal, 1986.

6. *On site experimental evaluation of a low-temperature solar organic rankine cycle system for RO desalination.* **D. Manolakos, G. Kosmadakis, S. Kyritsis, G. Papadakis.** s.l. : Solar Energy, 2009, Vol. 83, pp. 646–656.

7. *Optimization of low temperature solar thermal electric generation.* **Li Jing, Pei Gang, Ji Jie.** s.l. : Applied Energy, 2010, Vol. 87, pp. 3355–3365.

8. *A procedure to select working fluids for Solar Organic Rankine Cycles (ORCs).* **R., Rayegan and Y., Tao.** s.l. : Renewable Energy, 2010, pp. 1-12.

9. [Online] [Cited:] http://www.turboden.eu/en/Rankine/Rankine-history.php.

10. *Energetic and economic investigation of Organic Rankine Cycle applications.* **A. Schuster, S. Karellas, E. Kakaras, H. Spliethoff.** s.l. : Applied Thermal Engineering, 2009, Vol. 29, pp. 1809–1817.

11. **Ormat Technology Inc.** [Online] http://www.ormat.com/organic-rankine-cycle.

12. *Dynamic modeling and simulation of an Organic Rankine Cycle.* **Donghong Wei, Xuesheng Lu, Zhen Lu, Jianming Gu.** s.l. : Applied Thermal Engineering, 2008, Vol. 28, pp. 1216–1224.

13. *Design and testing of the Organic Rankine Cycle.* **T. Yamamoto, T. Furuhata, N. Arai, and K. Mori.** 3, March 2001, Energy, Vol. 26, pp. 239-251.

14. *Low-grade heat conversion into power using organic Rankine cycles – A review of various applications.* **B. F. Tchanche, G. Lambrinos, A. Frangoudakis, and G. Papadakis.** 8, s.l. : Renewable and Sustainable Energy Reviews, October 2011, Vol. 15, pp. 3963-3979.

15. *Fluid selection for a low-temperature solar organic Rankine cycle.* **B. F. Tchanche, G. Papadakis, G. Lambrinos, A. Frangoudakis.** 11-12, August 2009, Applied Thermal Engineering, Vol. 29, pp. 2468-2476.

16. *Analysis and optimization of the low-temperature solar organic Rankine cycle (ORC).* **A. M. Delgado-Torres, L. García-Rodríguez.** 12, December 2010, Energy Conversion and Management, Vol. 51, pp. 2846–2856.

17. *Performance analysis of an Organic Rankine Cycle with superheating under different heat source temperature conditions.* **J. P. Roy, M. K. Mishra, A. Misra.** 9, September 2011, Applied Energy, Vol. 88, pp. 2995–3004.

18. *Dynamic modeling and optimal control strategy of waste heat recovery Organic Rankine Cycles.* **S. Quoilin, R. Aumann, A. Grill, A. Schuster, V. Lemort, and H. Spliethoff.** 6, June 2011, Applied Energy, Vol. 88, pp. 2183-2190.

19. **ELECTRATHERM.** *Case studies.* [Online] [Cited: 30 10 2011.] http://electratherm.com/case_studies/solar_thermal_application_kona_hawaii/.

20. **CIESIN.** Chlorofluorocarbons and Ozone Depletion. *CIESIN Thematic Guides .* [Online] [Cited: 30 10 2011.] http://www.ciesin.columbia.edu/TG/OZ/cfcozn.html.

21. *Performance evaluation of a low-temperature solar Rankin cycle system utilizing R245fa.* **Wang W., Zhao L., Wang J., Zhang W., Zhao W. and Wu W.,.** 84 , s.l. : Solar Energy, 2010, pp. 353–364.

22. **NIST.** Chemistry web book. [Online] [Cited: 01 09 2011.] 2. http://webbook.nist.gov/cgi/fluid.cgi?ID=C460731&TUnit=K&PUnit=MPa&DUnit=mol%2Fl&HUnit=kJ%2Fmol&WUnit=m%2Fs&VisUnit=uPa*s&STUnit=N%2Fm&Type=IsoTherm&RefState=DEF&Action=Page.

23. **Joint Institute for Power and Nuclear Research.** *Thermo physical properties of R245fa.* Sosny : ASHRAE, 2004. Research Project 1256-RP.

24. **P., Holman J.** *Experimental methods for engineers.* New York : Mc Graw Hill, 2001.

25. *Development of property equations for butane and isobutane-preliminary design of an household regrigeration cycle. (M.Sc. Thesis).* **C., Gokhan.** METU-Ankara : s.n., 2009.

26. **Moran M., Shapiro H.** *Fundamentals of Engineering Thermodynamics; 6th edition.* New Jersey : Wiley, 2008.

27. **D., Incorpera F. and DeWitt.** *Fundamentals of heat and mass transfer.* New Jersey : Wiley, 1996.

28. **H., Kakac S. and Liu.** *Heat exchangers; Selection, rating and thermal design.* Florida : CRC Press, 2002.

29. **Y., Çengel.** *Heat transfer; A practical approach.* s.l. : McGraw Hill, 2008.

30. *Definition of an object oriented library for the dynamic simulation fo advanced energy systems: Methodologies, tools and application to combine ICE-ORC power plants (Phd dessertation).* **I., Vaja.** Genniao : UNIVERSITÀ DEGLI STUDI DI PARMA, 2009.

31. *An evaluation of prediction methods for saturated flow boiling heat transfer.* **Sun L., Mishima K.** 2009, s.l. : International Journal of Heat and Mass Transfer, Vol. 52, pp. 5323–5329.

32. *Power extraction from a hot stream in the presence of phase change.* **J.V.C. Vargas, J.C. Ordonez, A. Bejan.** 2000, International Journal of Heat and Mass Transfer , Vol. 43, p. 191±201.

33. **Kakaç, S.** *Boilers, evaporators, and condensers.* s.l. : Wiley-IEEE, 1991. ISBN 9780471621706.

34. *Performance and design optimization of a low-cost solar organic Rankine cycle for remote power generation.* **S. Quoilin, M. Orosz, H. Hemond, and V. Lemort.** 5, May 2011, Solar Energy, Vol. 85, pp. 955-966.

35. *Testing and modeling a scroll expander integrated into an Organic Rankine Cycle.* **V. Lemort, S. Quoilin, C. Cuevas, and J. Lebrun.** 14-15, October 2009, Applied Thermal Engineering, Vol. 29, pp. 3094-3102.

36. *A thermodynamic model for the analysis of screw expander performance.* **K. C. Ng, T. Y. Bong, and T. B. Lim.** 2, 1990, Heat Recovery Systems and CHP, Vol. 10, pp. 119-133.

37. *Optimization of low temperature solar thermal electric generation with Organic Rankine Cycle in different areas.* **L. Jing, P. Gang, and J. Jie.** 12, November 2010, Applied Energy, Vol. 87, pp. 3355-3365.
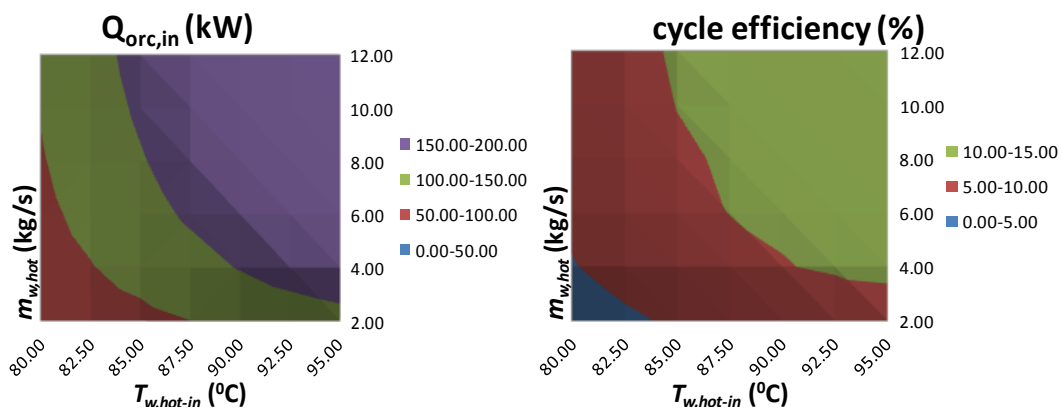
APPENDIX

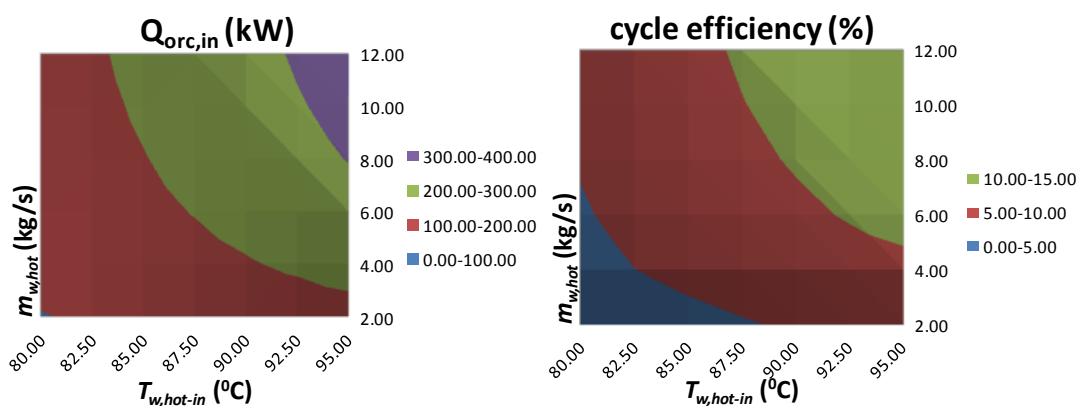Figure A. 1: Heat input and cycle efficiency for 0.75 kg/s refrigerant flow rate.

Figure A. 2: Heat input and cycle efficiency for 1.25 kg/s refrigerant flow rate.